

Rabi-like splitting and refractive index sensing with hybrid Tamm plasmon-cavity modes

S. Jena, R. B. Tokas, S. Thakur, and D. V. Udupa

Atomic & Molecular Physics Division, Bhabha Atomic Research Centre, Mumbai 400 085, India

* Corresponding author

E-mail addresses: shuvendujena9@gmail.com, shujena@barc.gov.in (S. Jena)

Abstract: We have theoretically demonstrated Rabi-like splitting and self-referenced refractive index sensing in hybrid plasmonic-1D photonic crystal structures. The coupling between Tamm plasmon and cavity photon modes are tuned by incorporating a low refractive index spacer layer close to the metallic layer to form their hybrid modes. Anticrossing observed in the dispersion validates the strong coupling between the modes and causes Rabi-like splitting, which is supported by coupled mode theory. The Rabi-like splitting energy decreases with increasing number of periods (N) and refractive index contrast (η) of the two dielectric materials used to make the 1D photonic crystals, and the observed variation is explained by an analytical model. The angular and polarization dependency of the hybrid modes shows that the polarization splitting of the lower hybrid mode is much stronger than that of the upper hybrid mode. Further investigating the hybrid modes, it is seen that one of the hybrid modes remains unchanged while other mode undergoes significant change with varying the cavity medium, which makes it useful for designing self-referenced refractive index sensors for sensing different analytes. For $\eta=1.333$ and $N=10$ in a hybrid structure, the sensitivity increases from 51 nm/RIU to 201 nm/RIU with increasing cavity thickness from 170 nm to 892 nm. For a fixed cavity thickness of 892 nm, the sensitivity increases from 201 nm/RIU to 259 nm/RIU by increasing η from 1.333 to 1.605. The sensing parameters such as detection accuracy, quality factor, and figure of merit for two different hybrid structures ($[\eta=1.333, N=10]$ and $[\eta=1.605, N=6]$) are evaluated and compared. The value of resonant reflectivity of one of the hybrid modes changes considerably with varying analyte medium which can also be used for refractive index sensing.

Key words: Tamm plasmon; Cavity mode, Strong coupling, Rabi splitting, Optical sensor

1. Introduction

Optical Tamm state (OTS) is a surface state which remains confined near the interface between two highly reflecting media. The sharp resonance in the measured reflection or absorption spectrum reveals the presence of OTS. If the OTS is confined near the interface between a 1DPC and a metallic layer, then it is called as Tamm plasmon (TP) which was theoretically proposed in 2007 [1] and experimentally observed in 2008 [2] by Kaliteevski *et al.* In contrast to surface plasmon resonance, the TP mode can be excited by both TE and TM polarized light irrespective of their angle of incidence. In recent years, the TP modes have gained wide attention due to their potential applications in optical filters, lasers, sensors and optical switches, heat emitters, and light-emitting devices [3-8]. The TP modes can be coupled with other resonant modes such as semiconductor excitons for applications in polaritonic devices [9], magnetic or surface plasmon for enhancing magnetic or electric field [10], microcavity modes for narrowband thermal emission [11], and defect modes for induced transparency [12]. The modes coupling generate “hybrid” modes in the system which is evident as a series of non-overlapping resonances in the reflection or absorption spectra. The resonance energies or wavelengths of the hybrid structures are primarily decided by the geometric parameters. The hybrid modes can exhibit interesting properties like Rabi splitting and can be utilized for refractive index sensing application.

When the resonant modes interact weakly, their coupled mode remains almost same like their bare resonant modes. Once the interaction becomes stronger, their coupled state generates new energy eigen values and exhibits entirely different optical properties as compared to their uncoupled or bare mode. The universal sign of strong coupling is the anticrossing of the modes in the dispersion curve when the modes approach each other. The energy gap between the modes at the anticrossing point is known as Rabi splitting, and the energy oscillation between the two modes is named as Rabi oscillation [13]. Generally, the strong localization of the TP mode makes strong coupling with the cavity modes, which is confirmed by Rabi-like splitting of the hybrid modes in analogy to cavity quantum-electrodynamic phenomena of Rabi splitting [14]. In quantum mechanics, when a quantum emitter (two-level atom or a quantum dot or a quantum well) having a specific excitons resonance is placed inside a micro/nano-cavity, the strong coupling between the transition of the two-levels and the cavity mode will result into two peaks (dips) in the transmission (reflection) spectrum, known as Rabi splitting [15]. Numerous experiments on Rabi splitting have been performed because of its potential applications in the atom detector and infrared photodetectors [16]. In recent years, Rabi-like splitting is explored in hybrid plasmon-exciton systems and hybrid photonic-plasmonic systems [17] for possible applications in various optoelectronic devices by controlling and tailoring the energy distribution [14]. In photonic-plasmonics systems, there has been significant attention on the hybrid modes formed due to simultaneous excitation of the TP mode and cavity mode. Das *et al.* [18] have recently shown the resonant and non-resonant coupling of microcavity mode and Tamm mode in carbon quantum dots embedded 1D photonic crystal structures both theoretically and experimentally.

The resonant modes have been tuned by changing the light polarization and by making wedge-shaped metallic layer across the photonic structure [19]. Generally, the modes splits into different linear polarizations termed as TE-TM splitting, which is crucial for phenomena like *all-optical* spin Hall Effect and anisotropic polarization flux [20]. Therefore, the study of modes coupling for different polarizations of light is very much essential and can be useful in applications of the enhanced light-matter interactions.

Coupling of resonant modes can be exploited to sharpen the resonances, which can be utilized for sensing and filtering applications. It is well known that the detection accuracy of the TP mode-based sensors is better as compared to that of the surface plasmon resonance (SPR) based sensors. Moreover, both the TP mode and the cavity mode can be excited for both transverse electric (TE) and transverse magnetic (TM) polarization of light in contrary to the SPR modes [21]. The SPR based sensors are less flexible for system portability and miniaturization because of its complex architecture involving gratings or high-index prisms [22]. Therefore, there have been growing interest in optical modes such as TP mode and cavity mode, and their hybrid modes. Ahmed *et al.* [6] have theoretically reported ultra-high sensitivity of 4784 nm/RIU using coupled Tamm/Fano resonant modes in porous silicon photonic crystal sensor. Shaban *et al.* [23] have experimentally reported sensitivity of 50 nm/RIU with signal to noise ratio of 0.46 in a multilayer Au/SiO₂/1D photonic crystal structure. But, these photonic structures do not exhibit self-reference sensing. Samir *et al.* [24] have theoretically realised a coupled TP polariton hybrid-mode based self-referenced refractive index sensor having variable sensitivity of 65 nm/RIU to 180 nm/RIU in the visible region. Most of the proposed hybrid modes-based sensors have very low thickness of analyte medium below 200 nm with sensitivity close to 200 RIU/nm. Submicron thickness analyte medium is very difficult to realize experimentally, therefore efforts have been made to enlarge the thickness of analyte medium with improved sensitivity in the present work.

Here, we have proposed a multilayer hybrid structure: metal/1DPC/cavity/1DPC *i.e.* Ag/(HL)^N/C/(HL)^N, which can be manipulated to show Rabi-like modes splitting and self-referenced refractive index sensing of analytes with desired sensing parameters. The strong coupling of TP and cavity modes with varying parameters of the structure such as period of the multilayer, refractive index contrast, thickness of spacer layer, incident angle, polarization of light, etc. have been thoroughly investigated. The hybrid structure is then optimized for refractive index sensing of analytes placed in the cavity having refractive index in the range of 1.33 to 1.49. Two hybrid structures are investigated in the present study for sensing applications. In one structure, the 1DPCs consists of low refractive index contrast materials ($\eta=1.333$) with $N=10$, while the other structure has 1DPCs with $\eta=1.605$ and $N=6$. The sensing parameters are estimated and compared for different thickness of the cavity medium for both the structures. The proposed hybrid structures would be useful in developing self-referenced optical sensors which can be easily integrated in any micro-systems as compared to the SPR based sensors.

2. Hybrid Tamm plasmon-cavity modes and theoretical formulation

Coupling of optically resonating modes are widely investigated in recent years. The most often studied coupled modes include microcavity mode and Tamm plasmon mode. The origin of both the modes and their unique features should be briefly discussed prior to exploring their coupling to form hybrid modes. Fig. 1(a) shows the schematic illustration of each modes and their hybrid modes. Cavity mode forms between a pair of 1DPCs (structure a₁). TP mode forms at the interface between a thin metallic layer and a 1DPC (structure a₂). Both modes are detected as a narrow resonance in the reflection spectrum but with different spatial electric field distribution. The optical energy is confined within the cavity layer, and localized at the metal/1DPC interface in case of cavity mode, and TP mode, respectively. Sharper the resonance in the spectrum, stronger is the field confinement in the desired structure. When these two individual structures a₁ and a₂ are merged, the modes are coupled to generate hybrid Tamm plasmon-cavity modes observed as two resonances in the reflection spectrum separated by a finite energy gap (structure a₃). In case of hybrid modes, the strong localization of the electric field intensity occurs both at the metal/1DPC interface and in the cavity layer. Fig. 1(b) shows the schematic of the hybrid photonic structure (Ag/Spacer layer/1DPC/Cavity/DPC), which is explored to investigate Rabi-like splitting of modes and refractive index sensing using such modes. The 1DPC consists of periodic layers of high index (H) and low index (L) materials with refractive index and thickness of (n_H, d_H) and (n_L, d_L), respectively. Spacer layer is a low index material (L), and the cavity layer parameters (n_c, d_c) are chosen as per the requirement. The cavity layer is placed between two 1DPC to form the microcavity structure.

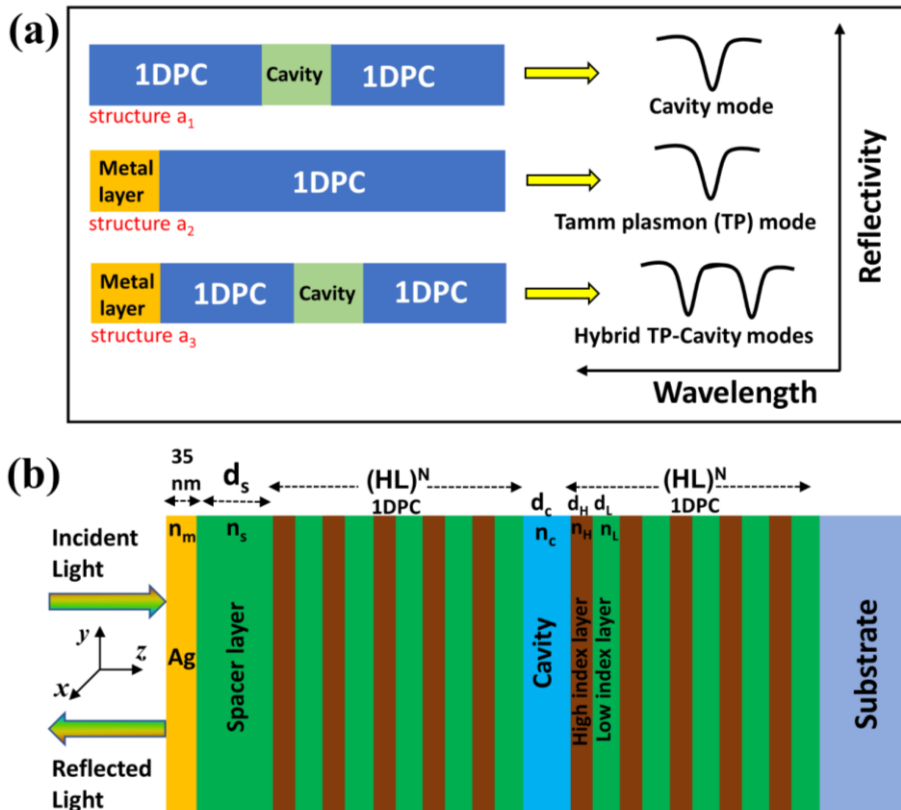


Fig. 1. (a) Step by step illustrations towards formation of hybrid Tamm plasmon-cavity modes. The structure a_1 forms cavity mode which is observed as a dip in the reflectivity spectrum in the photonic bandgap region. The structure a_2 forms Tamm plasmon mode which is observed as a dip in the reflectivity spectrum but with its energy confined at the metal/1DPC interface. The structure a_3 forms hybrid Tamm plasmon-cavity modes in which the above two photonic structures a_1 and a_2 are merged and they appear as a double dip in the reflectivity spectrum. **(b)** Schematic of hybrid photonic structure to investigate coupling of Tamm plasmon and cavity modes, and their utility for refractive index sensing application. The structure consists of a cavity/analyte layer sandwiched between two $(HL)^N$ 1DPCs with Ag metallic layer on top followed by a spacer layer. H and L stand for high and low refractive index materials respectively, and N stands for number of periods.

Modes coupling can be clearly understood from the sharp resonances in the optical reflection or transmission spectrum of the hybrid structure, which can be computed using transfer matrix method (TMM) [25-27]. In TMM, a multilayer consists of m layers with $m+1$ interfaces, and the right and left electric field components of a layer in the multilayer is related by a 2×2 matrix due to the fact the electric field wave equations are linear, and the tangential component of the electric field is continuous [25]. Each layer j ($j = 1, 2, 3, \dots, m$) has a thickness d_j and its complex refractive index is expressed as $\tilde{n}_j = n_j + ik_j$ which is a function of wavelength of light. The electric field components at ambient side ($j = 0$) and substrate side ($j = m+1$) are interrelated by the transfer matrix S as follows:

$$\begin{bmatrix} E_0^+ \\ E_0^- \end{bmatrix} = S \begin{bmatrix} E_{m+1}^+ \\ E_{m+1}^- \end{bmatrix} \quad (1)$$

where E_0^\pm and E_m^\pm are the electric field components travelling in the positive (+) and negative (-) direction at $j = 0$ and $j = m+1$, respectively. The transfer matrix (S) is obtained by multiplying refractive matrix $I_{j-1,j}$ of each interface and phase matrix L_j of each layer as follows [25]:

$$S = \begin{bmatrix} S_{11} & S_{12} \\ S_{21} & S_{22} \end{bmatrix} = \left(\prod_{j=1}^m I_{j-1,j} L_j \right) I_{m,m+1} \quad (2)$$

The refractive matrix or interface matrix between $(j-1)^{\text{th}}$ and j^{th} layers that describes refraction at q^{th} layer interface is given as follows

$$I_{j-1,j} = \frac{1}{t_{j-1,j}} \begin{bmatrix} 1 & r_{j-1,j} \\ r_{j-1,j} & 1 \end{bmatrix} \quad (3)$$

The phase matrix or layer matrix that describes propagation of electric field wave through q^{th} layer is given as follows

$$L_j = \begin{bmatrix} e^{-i\delta_j d_j} & 1 \\ 1 & e^{i\delta_j d_j} \end{bmatrix} \quad (4)$$

Here $t_{j-1,j} = 2y_{j-1}/(y_{j-1} + y_j)$ and $r_{j-1,j} = (y_{j-1} - y_j)/(y_{j-1} + y_j)$ are the complex Fresnel transmission and reflection co-efficient at $(j-1, j)$ interface, respectively, $y_j = \tilde{n}_j \cos \theta_j$ for S-polarized or TE waves, $y_j = \tilde{n}_j / \cos \theta_j$ for P-polarized or TM waves, $\delta_j = 2\pi\tilde{n}_j \cos \theta_j / \lambda$ is the

phase change experienced by the wave in travelling j^{th} layer, $\cos \theta_j = \sqrt{1 - (n_0 \sin \theta_0 / \tilde{n}_j)^2}$, $n_0 \approx 1$ is the refractive index of the incident medium (air), θ_0 is the angle of incidence, and θ_j is the angle of refraction in j^{th} layer [28]. The reflection and transmission co-efficient are given by $r = E_0^- / E_0^+ = S_{21} / S_{11}$ and $t = E_{m+1}^+ / E_0^+ = 1 / S_{11}$, respectively. Transmissivity and reflectivity of the multilayer structure are expressed as $T_M = |t|^2 \operatorname{Re}(\tilde{n}_{m+1}) / n_0$ and $R_M = |r|^2$, respectively. Typical thickness of glass substrates is in the range 0.5-10 mm $\gg \lambda$. Therefore, the reflection and transmission at the air-substrate and substrate-multilayer interfaces must be considered; consequently total transmission and total reflection of the multilayer/substrate system can be expressed as follows [29]:

$$T = \frac{T_S T_M e^{-2\beta_s}}{1 - R_S R_M e^{-4\beta_s}} \quad (5)$$

$$R = R_M + \frac{R_S T_M^2 e^{-4\beta_s}}{1 - R_S R_M e^{-4\beta_s}} \quad (6)$$

where $T_S = |4n_0 \tilde{n}_{m+1} / (n_0 + \tilde{n}_{m+1})^2|$ and $R_S = |(n_0 - \tilde{n}_{m+1})^2 / (n_0 + \tilde{n}_{m+1})^2|$ are transmission and reflection, respectively at substrate-air interface, $\tilde{n}_{m+1} = \tilde{n}_s = n_s + ik_s$ is the complex refractive index of the substrate, $\beta_s = 2\pi k_s d_s / \lambda$ is the phase thickness related to absorption in the substrate. k_s and d_s are the extinction co-efficient and thickness of the substrate, respectively.

The electric field within any arbitrary layer q is computed by considering the division of the multilayer structure into two subsections separated by the layer q , as a result the total system transfer matrix can be expressed as [30]

$$S = S_q' L_q S_q'' \quad (7)$$

$$\text{with } S_q' = \begin{bmatrix} S_{q11}' & S_{q12}' \\ S_{q21}' & S_{q22}' \end{bmatrix} = \left(\prod_{j=1}^{q-1} I_{j-1,j} L_j \right) I_{q-1,q} \quad (8)$$

$$\text{and } S_q'' = \begin{bmatrix} S_{q11}'' & S_{q12}'' \\ S_{q21}'' & S_{q22}'' \end{bmatrix} = \left(\prod_{j=q+1}^m I_{j-1,j} L_j \right) I_{m,m+1} \quad (9)$$

The complex reflection and transmission co-efficient of layer q in terms of matrix elements can be defined as $r_q^+ = S_{q21}' / S_{q11}'$, $r_{q-}^+ = -S_{q12}' / S_{q11}'$, $t_q^+ = 1 / S_{q11}'$, $r_q^- = S_{q21}'' / S_{q11}''$ and $t_q^- = 1 / S_{q11}''$. The electric field travelling in the forward (positive) and backward (negative) direction in the layer q at the left interface ($q-1, q$) is connected to the incident plane wave E_0^+ as follows [25]:

$$t_q^+ = \frac{E_q^+}{E_0^+} = \frac{t_q^+}{1 - r_{q-}^+ r_q^+ e^{i2\delta_q d_q}} \quad (10)$$

$$t_q^- = \frac{E_q^-}{E_0^+} = \frac{t_q^- r_q^- e^{i2\delta_q d_q}}{1 - r_{q-}^- r_q^- e^{i2\delta_q d_q}} = t_q^+ r_q^- e^{i2\delta_q d_q} \quad (11)$$

Using equation (10) and (11), the depth (z) dependent electric field distribution in any arbitrary position in q^{th} layer can be expressed in terms of incident plane wave E_0^+ as follows

$$E_q(z) = E_q^+(z) + E_q^-(z) = [t_q^+ e^{i\delta_q z} + t_q^- e^{-i\delta_q z}] E_0^+ \quad (12)$$

The normalized electric field intensity is estimated using Eq. (12). The spatial localization of the electric fields in the multilayer confirms the existence of optical Tamm mode or cavity mode or their coupled modes, therefore electric field distribution is an essential parameter that needs to be determined for analyzing the modes present in the hybrid structure.

3. Results and discussion

The plasmonic-photonic crystal heterostructure as shown in Fig. 1(b) is systematically analysed to realise Rabi-like splitting, and refractive index sensing using the hybrid modes, which are discussed below in detail. Rabi-like splitting is expressed considering reflectivity as a function of energy of the light, while refractive index sensing is better described expressing reflectivity as a function of wavelength. It is chosen for convenience to better explain the phenomena of the hybrid modes as one can be converted to other through the relation $\text{Energy} = \hbar\omega = hc/\lambda$, where ω and λ are the angular frequency and wavelength of light, respectively.

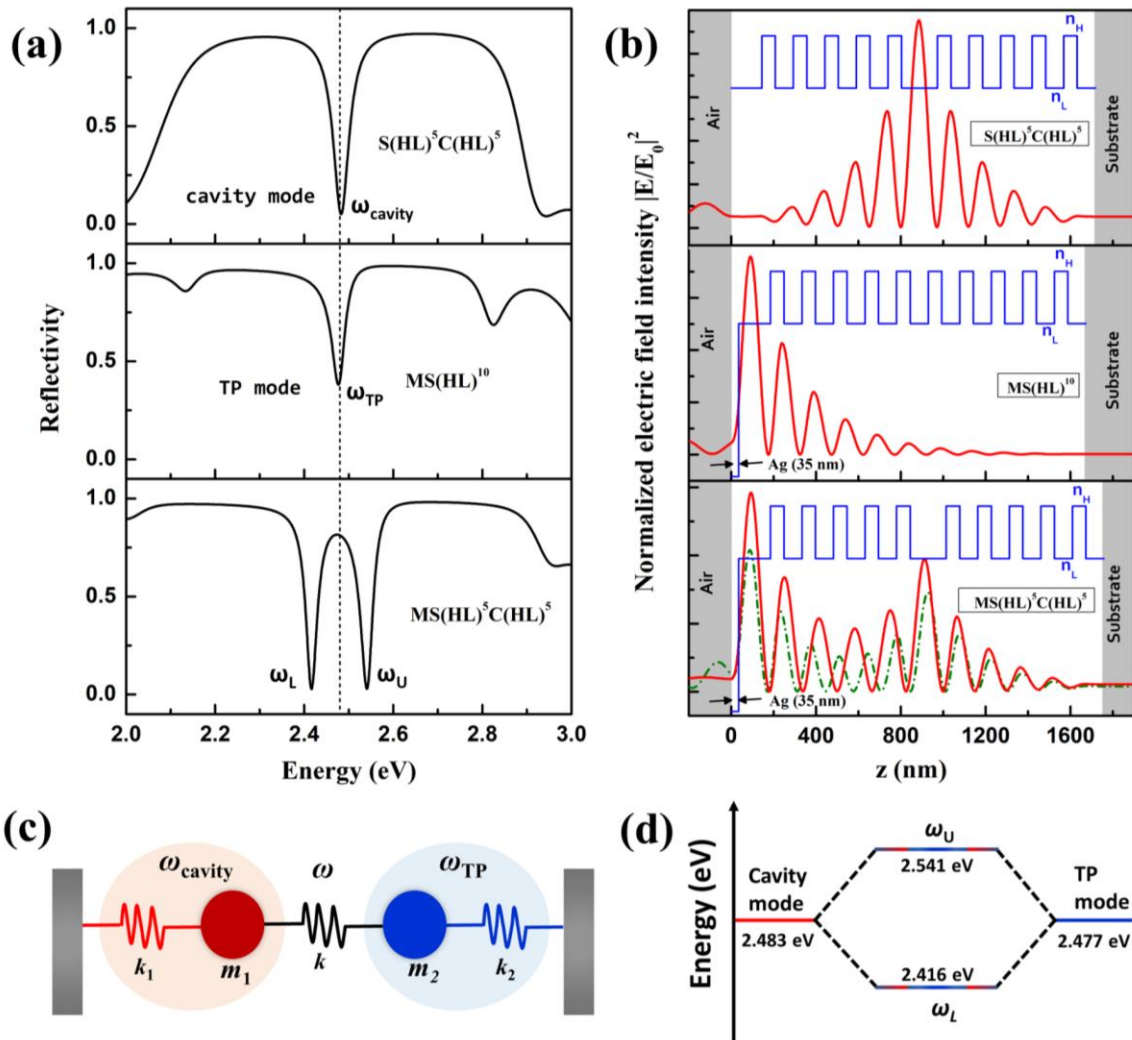


Fig. 2. Proposed hybrid structure is $MS(HL)^5C(HL)^5$, where M is Ag thin layer having thickness $d_m=35$ nm, H is a high index ($n_H=1.96$) thin layer having thickness $d_H=64$ nm, L is a low index ($n_L=1.47$) thin layer having thickness $d_L=85$ nm, S is a low index ($n_S=1.47$) spacer layer having thickness $d_S=141$ nm, and C is a cavity layer having thickness $d_C=85$ nm filled with medium having refractive index $n_c=1.47$. **(a)** Reflection spectra of photonic structure without metallic layer (bare cavity mode), without cavity layer (TP mode), and with both metallic and cavity layers (hybrid TP-cavity modes), respectively. **(b)** The refractive index profile and the normalized electric field intensity distribution in the top plot corresponds to the cavity mode localized between two 1DPCs at light energy of 2.483 eV, the middle plot corresponds to the Tamm-plasmon mode localized at the interface between Ag layer and a 1DPC at light energy of 2.477 eV, and the bottom plot corresponds to the hybrid Tamm plasmon-cavity modes at $\omega_L=2.416$ eV (dotted green line) and $\omega_U=2.541$ eV (solid red line), respectively. Schematic of **(c)** coupled oscillator model, and **(d)** energy diagram for coupling between TP and cavity modes.

3.1. Modes coupling

The hybrid photonic structure (schematic shown in Fig. 1(b)) for tunable modes-coupling consists of thin Ag layer followed by low index spacing layer covering a cavity structure made of a low index layer sandwiched between two 1DPCs placed on a transparent glass substrate. The 1DPC structure comprises $N=5$ periods of alternative high index (H)/low index (L) layers. The hybrid heterostructure is: $Ag/S/(HL)^5/C/(HL)^5/Substrate$. The refractive index of both S and C layers is same i.e. $n_c=n_S=1.47$. The thickness values of Ag layer, S layer, and C layer are $d_m=35$ nm, $d_S=141$ nm, and $d_C=85$ nm, respectively. Both the H and L layers are assumed as lossless and dispersion free dielectrics with refractive index and thickness values of ($n_H=1.96$, $d_H=64$ nm) and ($n_L=1.47$, $d_L=85$ nm), respectively. The complex permittivity of Ag as a function of frequency is determined using Drude model as $\epsilon_{Ag}(\omega)=\epsilon_\infty - [\omega_p^2/(\omega^2 - i\omega\gamma)]$, where $\epsilon_\infty = 3.4$ is the high-frequency dielectric constant, $\omega_p=1.39\times 10^{16}$ rad/s is the plasma frequency, and $\gamma=2.7\times 10^{13}$ rad/s is the scattering rate that represents the absorption nature of the metallic layer.

Fig. 2(a) shows the calculated reflection spectra of $MS(HL)^5C(HL)^5$ structure without M layer, without C layer, and with both M and C layers, respectively. The photonic bandgap lies in the energy range of 2.2-2.7 eV with centre at ~ 2.48 eV. The optimized thickness values of M layer (Ag) and S layer are 35 nm and 141 nm, respectively, in order to obtain desired TP mode at the centre of the photonic bandgap. Without spacing layer, the TP mode significantly deviates from the resonant cavity mode (see supplementary material Fig. S1), as a result the coupling between the TP mode and cavity mode becomes poor. Therefore, the spacing layer thickness is very crucial for strong coupling of modes. The TP mode is also very sensitive to M layer thickness (see supplementary material Fig. S2). When thickness of the metallic layer is more than its skin depth, then the layer does not transmit much light through it, consequently the structure does not support the TP mode at the metal/1DPC interface due to insufficient light. When the thickness is less than the skin depth, the light pass through the M layer and the TP mode appears at the metal/1DPC interface. The TP mode undergoes red-shift with decreasing M layer thickness, and then disappears when the M layer thickness is such that it does not reflect sufficient light to sustain the mode at the interface. Therefore, the optimized value of M layer thickness is prerequisite for sustaining TP mode which is 35 nm in the present

structure. Similarly, the thickness of S layer is also equally important for sustaining the TP mode at the desired energy or wavelength, and the optimized thickness of S layer is $d_s=141$ nm (see supplementary material Fig. S3). The resonance in the reflection spectrum generates a dip at 2.483 eV and 2.477 eV for cavity mode without M layer and TP mode without C layer, respectively, close to the centre of the bandgap. The reflectivity is around 1% with C layer, while it is around 40% with M layer around 2.48 eV. The high reflectivity of the Ag metallic layer makes the dip smaller in case of TP mode. In case of $MS(HL)^5C(HL)^5$ structure with both M and C layers, one expects that the two modes will be merged to give a sharper resonant reflectivity at the central energy of around ~2.48 eV. But the modes are strongly coupled in such a way that there is no resonance reflection at 2.48 eV, instead generates two resonant hybrid modes at 2.416 and 2.541, respectively symmetric around 2.48 eV. The properties of hybrid TP-cavity modes are entirely different from their individual uncoupled modes. The spatial confinement of such modes can be established by numerically estimating electric field intensity. Fig. 2(b) shows the electric field intensity distribution for the $S(HL)^5C(HL)^5$ structure (cavity mode at 2.483 eV), $MS(HL)^{10}$ structure (TP mode at 2.477 eV), and $MS(HL)^5C(HL)^5$ structure (hybrid TP-cavity modes at 2.541 eV and 2.416 eV). The electric field intensity at cavity mode of 2.483 eV is found spatially localized in the cavity C layer of the $S(HL)^5C(HL)^5$ structure, confirms the presence of cavity mode formed between the two $(HL)^5$ 1DPCs. The electric field intensity at TP mode of 2.477 eV is found spatially localized in the S layer of $MS(HL)^5C(HL)^5$ structure, confirms the presence of TP mode formed between the M layer and the $(HL)^5$ 1DPC. It shows that TP mode is a surface mode that propagates along the surface unlike the cavity mode where the light is confined within the cavity layer of the structure. The electric field intensity at the two resonant hybrid modes of 2.541 eV and 2.416 eV is found localized both at the metal/1DPC interface, and in the cavity layer of the $MS(HL)^5C(HL)^5$ structure. The M layer thickness dependent reflectivity calculation indicates (see supplementary material Fig. S2) that, the energy $\omega_U=2.541$ eV corresponds to the cavity mode part whereas the energy $\omega_L=2.416$ eV corresponds to TP mode part of the hybrid TP-cavity modes. The value of electric field intensity localized in the S layer as well as C layer for 2.541 eV is higher as compared to that for 2.416 eV. The field confinement both in the S and C layer clearly indicates that the TP and cavity modes are strongly coupled in the exact crossing region. The hybrid TP-cavity modes can be classically represented by two coupled oscillators having uncoupled energy Eigen values ω_{cavity} and ω_{TP} , respectively as shown in the Fig. 2(c). The strong interaction between bare cavity and bare TP modes generate hybrid mode energy levels (ω_U and ω_L) as shown in Fig. 2 (d) that are indistinguishable unlike in their uncoupled mode, and exhibits entirely new features.

The coupling of hybrid modes has been tuned by varying thickness of spacing layer d_s . The reflectivity as a function of energy and d_s of the hybrid structure is plotted in contour Fig. 3 (a). It shows that there is an anticrossing of the two modes (ω_U and ω_L) at a specific value of $d_s=141$ nm resulting Rabi-like splitting of the modes. The detail of the coupled modes is illustrated in Fig. 3(b) which shows the variation of bare TP mode, bare cavity mode, and their

coupled hybrid modes as a function of d_s . The bare cavity mode exhibits redshift with increasing d_s , while the bare cavity mode does not change with d_s and remains fixed at 2.486 eV. However, the results in case of coupled modes in hybrid photonic structure are very interesting. The hybrid modes (ω_U and ω_L) deviate from their bare TP and cavity modes in the strong coupling region *i.e.* $130 \text{ nm} \leq d_s \leq 150 \text{ nm}$, while their variation with d_s is similar to that of the bare modes in either side of the strong coupling region. The TP mode and the cavity mode strongly repel each other away from their almost unique bare mode energy of ~ 2.48 eV for $d_s=141$ nm, which results to the anticrossing of the two modes as they become closer. This anticrossing is the indication of strong coupling. The TP-cavity hybrid modes ω_U and ω_L are located at the energy of 2.416 eV and 2.541 eV, respectively. The separation between the two modes ω_U and ω_L exactly at the anticrossing region is 125 meV, known as Rabi-like splitting. The splitting energy is considerable greater than their bare mode linewidth, which further confirms the occurrence of strong coupling between TP and cavity modes [31]. Therefore, coupling between the TP mode and the cavity mode in a hybrid photonic structure can be made either strong or weak by varying S layer thickness.

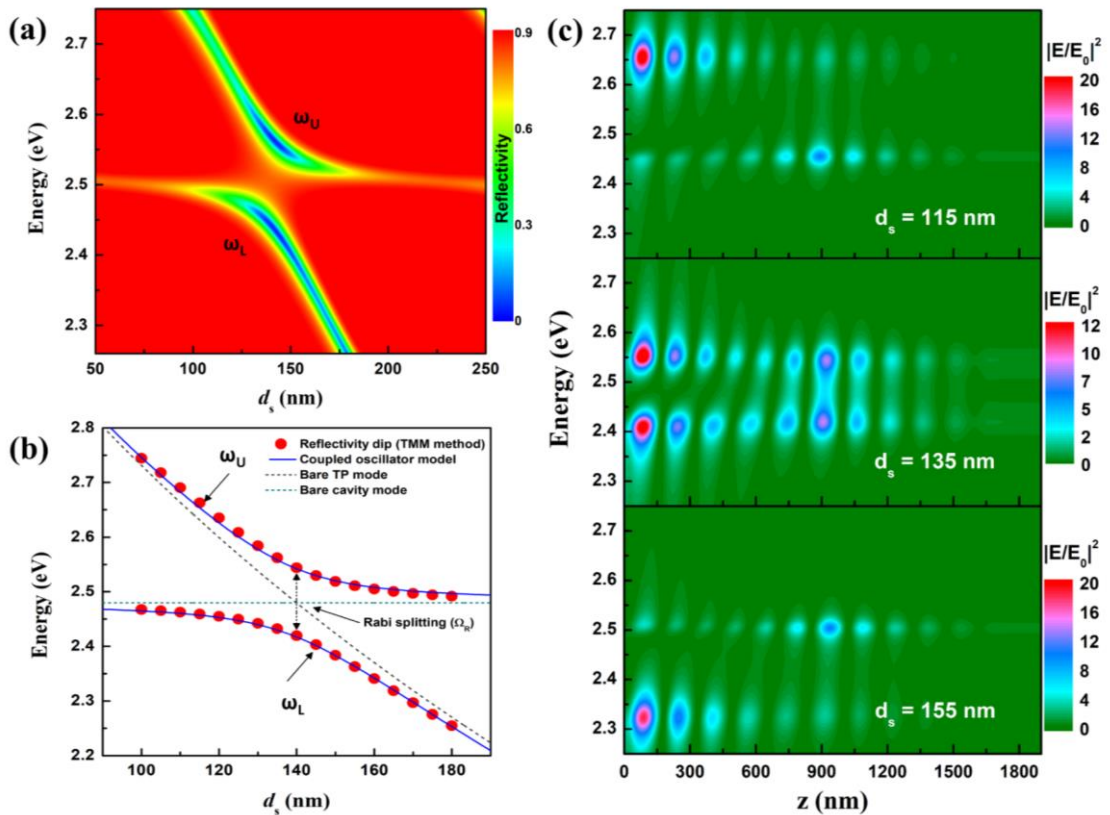


Fig. 3. (a) Reflectivity contour of the hybrid structure as a function of incident light energy and S layer thickness d_s . (b) Solid red circles represent the positions of the reflectivity dip of the hybrid modes as a function of d_s obtained using TMM and are fitted using coupled oscillator model (solid blue line). The computed bare TP mode (dotted grey line) and bare cavity mode (dotted cyan line) are also presented. (c) Normalized electric field intensity $|E/E_0|^2$ (arb. unit) as a function of energy and depth (z) in the structure for three different values of $d_s = 115 \text{ nm}$, 135 nm , and 155 nm around the coupling region.

The modes coupling in the hybrid structure can be better understood by considering coupled oscillator model. The TP mode and the cavity mode can be considered as two

oscillators coupled in the hybrid structure. The energy Eigen values (ω) of the coupled oscillators can be obtained by solving the following equation [32]:

$$\begin{vmatrix} \omega - \omega_{cavity} & \Omega_{cT} \\ \Omega_{cT} & \omega - \omega_{TP} \end{vmatrix} = 0 \quad (13)$$

where ω_{cavity} and ω_{TP} are the eigen energies of the bare cavity mode and bare TP mode, respectively. Ω_{cT} is the coupling strength between the two bare modes. From equation (13), we can get

$$(\omega - \omega_{cavity})(\omega - \omega_{TP}) = \Omega_{cT}^2 \quad (14)$$

The spacing layer thickness d_s close to the Ag metallic layer is adjusted to tune the TP mode. Therefore, ω_{TP} is considered as a function of d_s *i.e.* $\omega_{TP}(d_s)$. Hence, the two solutions of the quadratic equation (14) can be expressed as follows:

$$\omega_U(d_s) = \frac{1}{2} \left[(\omega_{cavity} + \omega_{TP}(d_s)) + \sqrt{(\omega_{cavity} - \omega_{TP}(d_s))^2 + 4\Omega_{cT}^2} \right] \quad (15)$$

$$\omega_L(d_s) = \frac{1}{2} \left[(\omega_{cavity} + \omega_{TP}(d_s)) - \sqrt{(\omega_{cavity} - \omega_{TP}(d_s))^2 + 4\Omega_{cT}^2} \right] \quad (16)$$

The upper and lower hybrid modes have been theoretically fitted using equation (15) and (16), respectively as shown in Fig. 3 (b). This shows that the resonant energies of the hybrid modes obtained using coupled oscillators model are in excellent agreement with that of the values obtained from transfer matrix method. The upper hybrid mode ω_U behaves like TP mode for lower d_s values, and gradually changes to behave like cavity mode with increasing d_s value. The lower hybrid mode ω_L behaves like cavity mode for lower d_s values, and gradually changes to behave like TP mode for increasing d_s value. It shows that thickness of spacer layer d_s is very crucial in determining the properties of the hybrid modes. Hence, the spacer layer acts as a modulator for tailoring the modes of the coupled system. The mechanism behind this can be better understood by analysing the electric field intensity in the structure. Therefore, we have chosen three values of d_s : 115 nm, 135 nm, and 155 nm. The thickness values (115 nm and 155 nm) are lower, and higher than the strong coupling thickness region, while the thickness of 135 nm is in the strong coupling region. In order to compare the effect of d_s , the electric field distribution as a function of energy and depth (z) for the three d_s values are plotted in Fig. 3(c). For $d_s=115$ nm, the modes are uncoupled, and the cavity mode is completely suppressed for the uncoupled upper energy mode, while the TP mode is completely absent in case of the uncoupled lower energy mode. The observations are entirely opposite for $d_s=155$ nm. The modes are strongly coupled for $d_s=135$ nm, and the amplitude of TP mode is larger than that of the cavity mode for both the lower as well as upper energy modes. It shows that there exists a competing phenomenon between the two modes in their coupled states.

3.2. Rabi-like splitting

The TP and cavity modes are allowed to couple around a common energy by choosing optimized spacing layer thickness $d_s=141$ nm, consequently they exhibit Rabi-like splitting in

the strong coupling region where the gap between upper and lower mode becomes minimum. This minimum gap energy is known as Rabi energy (Ω_R). It is seen that Rabi energy varies with change in number of periods (N) and refractive index contrast between the dielectric layers (η) in the 1DPC. The variation of hybrid TP-cavity modes with number of periods (N) in the $(HL)^N$ 1DPC for a given refractive index contrast of $\eta=n_H/n_L=1.96/1.47=1.33$ has been numerically estimated and plotted in Fig. 4(a). The figure shows that the linewidth of the resonant coupled modes becomes narrower with increasing N values. The resonant reflectivity value increases with increasing N, but the value remains same for both the hybrid modes. The value of Ω_R decreases dramatically with increasing N values, and becomes almost constant for higher value of N as shown in Fig. 4(c). The reflectivity of the hybrid structure with increasing value of η for a fixed value of N=5 has been calculated and plotted in Fig. 4(b). The trend of variation of Ω_R in hybrid modes with η is almost identical to that of N as shown in Fig. 4(d).

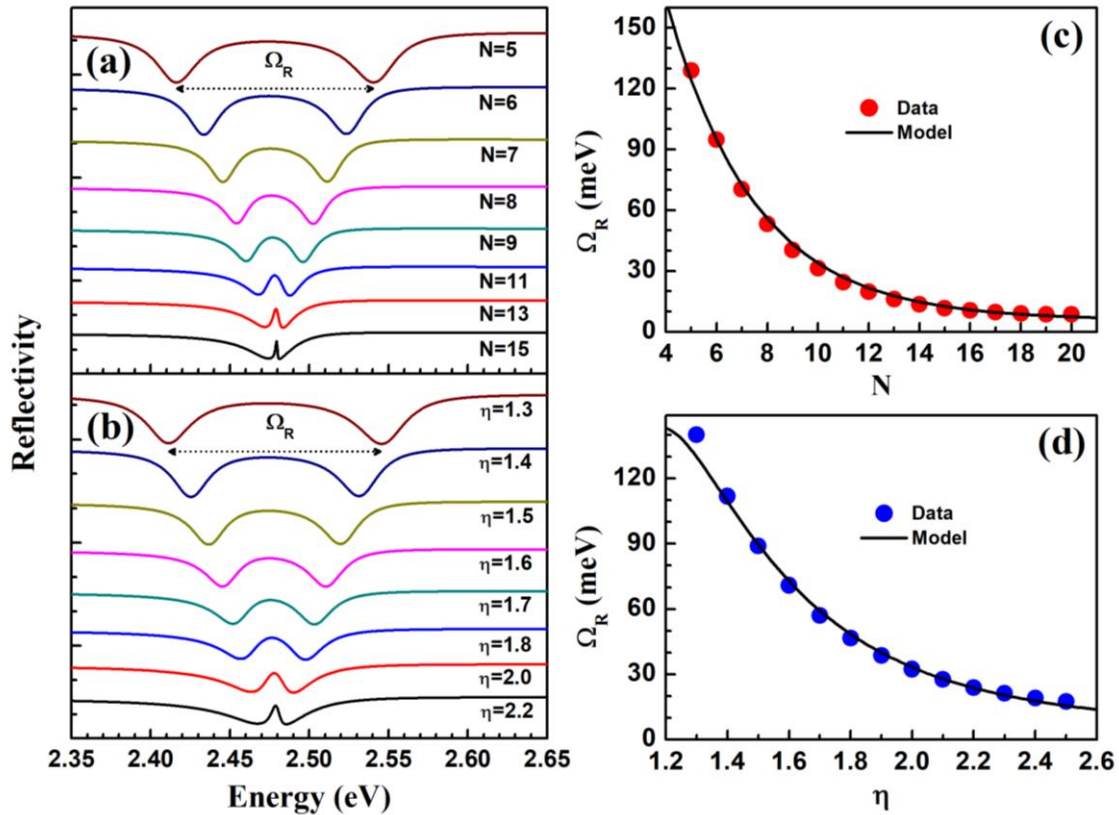


Fig. 4. Reflection spectra of the hybrid photonic structure (a) with varying number of period N for a fixed value of $\eta=1.333$, and (b) with varying refractive index contrast η for a fixed value of N=5. The energy separation between the two dips marked with a double-arrow line is the Rabi-like splitting energy (Ω_R). Variation of Ω_R as a function of (c) N, and (d) η . The solid black line curves (—) in both the plot c and d are calculated using equation (24) with varying N and η , respectively.

The variation of Rabi-like splitting with N and η has been described using an analytical model, which is based on transfer matrix elements for complex amplitudes of forward and backward propagating waves as follows [33]:

$$A \begin{pmatrix} 1 \\ r_R \end{pmatrix} = \begin{pmatrix} e^{i\varphi_c} & 0 \\ 0 & e^{-i\varphi_c} \end{pmatrix} \begin{pmatrix} t^2 - r^2 & r \\ -r & 1 \end{pmatrix} \begin{pmatrix} e^{i\varphi_s} & 0 \\ 0 & e^{-i\varphi_s} \end{pmatrix} \begin{pmatrix} r_M \\ 1 \end{pmatrix} \quad (17)$$

where A is a constant, φ_s is the phase factor due to the dielectric spacer layer, φ_c is the phase factor due to the cavity, t and r are the transmission and reflection amplitude co-efficient of the left 1DPC, r_R is the reflection amplitude co-efficient of the right 1DPC, and r_M is the reflection amplitude co-efficient of the metal layer. Eliminating A from the two algebraic equations of Eq. (17) gives

$$\left[1 - (rr_M e^{2i\varphi_s})^{-1}\right] \left[1 - (rr_R e^{2i\varphi_c})^{-1}\right] = t^2/r^2 \quad (18)$$

Since plasma frequency ω_p of the metal is much larger than the frequency of light considered in the present case (visible light), therefore r_M can be approximately expressed as

$$r_M \approx \exp \left[i \left(\pi + \frac{2\omega n_L}{\omega_p \sqrt{\varepsilon_b}} \right) \right] \quad (19)$$

where ε_b is the real part of the dielectric permittivity of the metallic layer. For frequencies close to the centre of the PBG, the value of r_R and r can be approximately given by

$$r_R \approx r \approx \exp \left[i\beta \left(\frac{\omega - \omega_0}{\omega_0} \right) \right] \quad (20)$$

where $\beta = \pi/(\eta-1)$ and ω_0 is the central frequency of the PBG. The right-hand side of Eq. (18) can be approximated by

$$t^2/r^2 \approx -4(1/\eta)^{2N} \quad (21)$$

For $\omega \approx \omega_0$ and $\omega < \omega_p$, Eq. (18) can be expressed as linear function of ω and can be reorganized in the form of Eq. (14) as

$$(\omega - \omega_{cavity})(\omega - \omega_{TP}) = \Omega_{cT}^2 \quad (22)$$

For $\omega_{TP} \approx \omega_0$, the value of Ω_{cT} is given by [33]

$$\Omega_{cT} = \frac{1}{\pi} \left(\frac{1}{\eta} \right)^N \left[\frac{1 - (1/\eta)}{\sqrt{1 - (1/2\eta)}} \right] \omega_0 \quad (23)$$

The Rabi-like splitting energy (Ω_R) is double of Ω_{cT} and is given by

$$\Omega_R = 2\Omega_{cT} = \frac{2}{\pi} \left(\frac{1}{\eta} \right)^N \left[\frac{1 - (1/\eta)}{\sqrt{1 - (1/2\eta)}} \right] \omega_0 \quad (24)$$

where $\eta = n_H/n_L$ is the refractive index contrast, and N is the number of periods in the 1DPC. Equation (24) is independent of properties of metallic layer. The analytically obtained values of Ω_R using equation (24) for varying N and η are exactly matching with that of numerically obtained values as shown in Fig. 4(c) and (d), respectively. The Rabi energy can be reach up to 125 meV for $N=5$, which exhibits strong coupling. For lower N value, the resonant electric field corresponding to the TP mode easily passes through the 1DPC, and efficiently interacts with the cavity mode resulting large value of Rabi-like splitting energy. There is an exchange of energy between the cavity layer and metallic silver interface (close to S layer) because of strong coupling of cavity and TP modes, as a result enhanced light-matter interaction occurs in either of the C and S layers. Strong interaction between cavity mode and TP mode can also be

made by choosing dielectric layers with lower η value for a fixed value of N , that is why large value of Ω_R is obtained for lower value of η as shown in Fig. 4(d). The value of Ω_R decreases with increasing η for the hybrid photonic structure. The effect of η on the interaction of the cavity and TP modes in the coupled state is exactly identical to that of the effect of N . The role of N and η in a hybrid structure are interrelated and their combination can be optimized as per the desired interaction of the modes in the strong coupling region.

3.3. Polarization splitting

The variation of hybrid modes with varying angle of incidence for both TE and TM polarized light have been numerically estimated and plotted in Fig. 5(a). It is found that both the hybrid modes ω_U and ω_L exhibit identical parabolic dispersion curve irrespective of polarization of light, which ensures the strong coupling between the cavity and TP modes. The resonant hybrid modes undergo blueshift to the higher energy with increasing angle of incidence. Because, the resonant energy of the modes must increase to maintain a fixed phase shift (δ) following the resonance condition $\delta = 2\pi n d \cos \theta / \lambda$, where d is the virtual cavity thickness. The value of resonant reflectivity dip and its bandwidth of both the modes remain constant over a wider angle range up to nearly 25° . The value of reflectivity dip of the TM-polarized light for the hybrid modes remain unchanged over a wide angular region, which makes it useful for developing dual-narrow-band and tunable reflection in this region. The polarization splitting (TM-TE) for both the modes increase quadratically with increasing angle of incidence as shown in Fig. 5(b). The value of polarization splitting is higher for low energy mode ω_L as compared to that of ω_U and it becomes larger towards high angles of incidence. The estimated splitting value reaches up to 114 meV for ω_L and 9 meV for ω_U , respectively at angle of $\theta=70^\circ$. It is seen that the polarization splitting can be tuned by varying either thickness of metallic layer or spacing layer or both [34]. The polarisation dependent coupling of Tamm plasmon and cavity modes provides better understandings about the mode structure. It shows that sharp hybrid resonant modes of orthogonal polarization can be tuned as per the requirement, which could be useful for optoelectronic device applications.

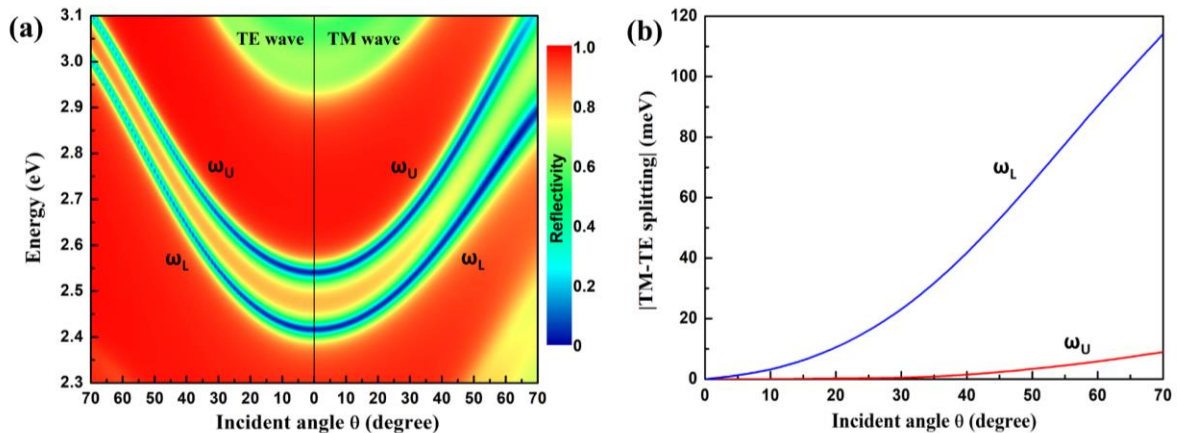


Fig. 5. (a) Reflectivity contour as a function of energy and incident angle for TE and TM-polarized light, respectively. (b) Splitting between TE and TM-polarizations as a function of incident angle for the hybrid TP-cavity modes.

3.4. Refractive index sensing

The hybrid modes in the plasmonic-photonic crystal heterostructure can be utilized for refractive index sensing applications considering the fact that at least one of the modes must be sensitive to the change in the cavity medium. The objective is to sense refractive index values from 1.33 to 1.49 using the hybrid modes as this range covers the refractive indices of most of the biochemical samples, and therefore can be used for biochemical sensing. In that context, a sensing configuration has been designed in which two photonic structures PS1 and PS2 are kept at submicron level thick apart forming a cavity as shown in Fig. 6 (a). The structure of PS1 is substrate/Ag/1DPC, while that of PS2 is 1DPC/substrate. The cavity is filled with analytes to be sensed. An experimental set-up has been proposed whose schematic is shown in Fig. 6 (b). In this set-up, UV-VIS-NIR light from the light source is sent through multiple illumination fibres to the hybrid structure (PS1/cavity/PS2) and the reflected light is collected by another optical fibre in the centre of the reflection probe which is coupled to a spectrometer. A fluid flow channel passing through the cavity can be designed for the sensing scheme as described elsewhere [35-37].

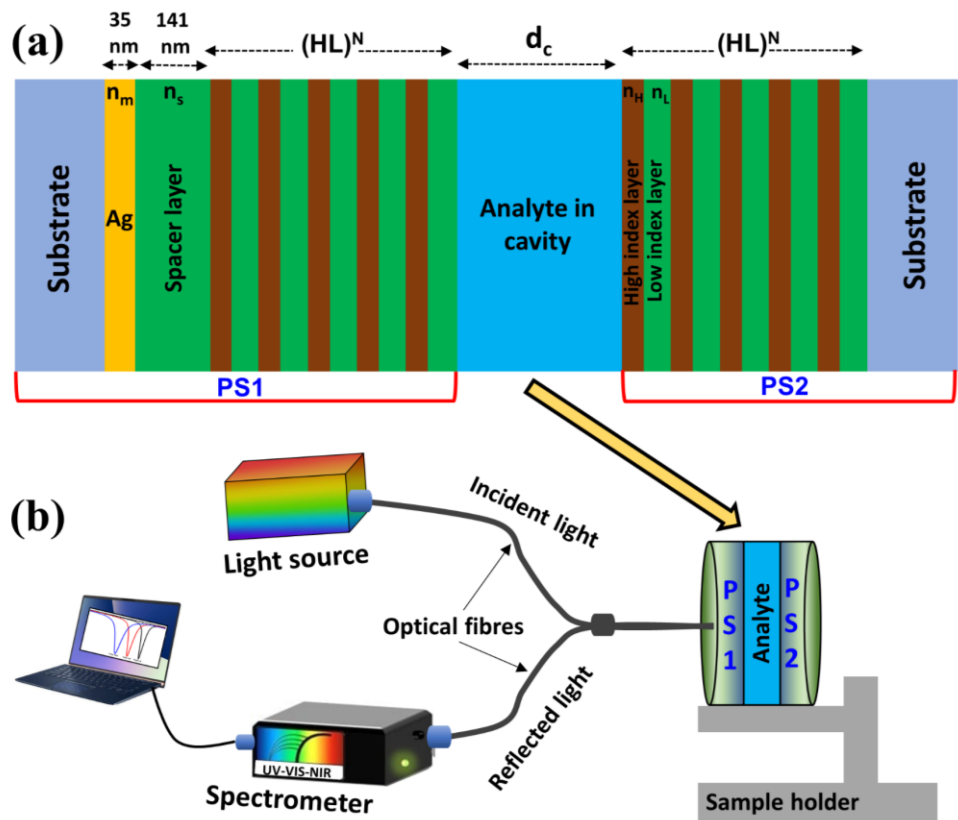


Fig. 6: (a) Schematic of hybrid photonic structure as a refractive index sensor. It consists of an analyte medium in the cavity between two photonic structures PS1 and PS2. (b) Proposed experimental set-up for sensing refractive index of the analyte medium.

Now, the calculations have been done to see how sensitive the hybrid modes are with varying analyte medium. It is found that the designed hybrid plasmonic-photonic structure can give better sensitivity and performance of the sensors, which is mentioned step by step as follows. At first, the behaviour of resonant modes with varying cavity (analyte) thickness has

been investigated for two hybrid structures S1 and S2 having different values of η and N in the 1DPCs. The structure S1 is designed as $\text{Ag}/\text{SiO}_2/(\text{HfO}_2/\text{SiO}_2)^{10}/\text{Analyte}/(\text{HfO}_2/\text{SiO}_2)^{10}/\text{Glass}$ with $\eta=1.333$ ($n_{\text{HfO}_2}/n_{\text{SiO}_2}=1.96/1.47$) and $N=10$. The structure S2 is designed as $\text{Ag}/\text{SiO}_2/(\text{TiO}_2/\text{SiO}_2)^6/\text{Analyte}/(\text{TiO}_2/\text{SiO}_2)^6/\text{Glass}$ with $\eta=1.605$ ($n_{\text{TiO}_2}/n_{\text{SiO}_2}=2.36/1.47$) and $N=6$. The value of N in both structures is optimized to obtain sharp resonant mode which is sensitive to the change in the analyte medium. The reflectivity contour of S1 structure as a function of wavelength and cavity thickness for two extreme analyte refractive index values $n=1.33$ and 1.49 are plotted in the Fig. 7, while that for S2 structure is provided in the supplementary material (see Fig. S5). The figure shows the strong coupling between the TP mode and cavity mode as evident from the anticrossing or splitting of the modes at different value of cavity thickness. The resonant mode λ_a significantly varies with analyte thickness, while that of λ_R almost remains unchanged except at and around the strong coupling region. For sensing point of view, one should avoid the cavity thickness values for which the strong coupling occurs. Therefore, the five values of cavity thickness ($d_c=170$ nm, 340 nm, 510 nm, 705 nm, and 892 nm) for which one mode remains fixed while other modes change largely has been chosen for refractive index sensing. There exist multiple analyte modes for a given values of d_c as marked by arrows: one is above and other is below λ_R . One can use either of them or both for refractive index sensing purposes.

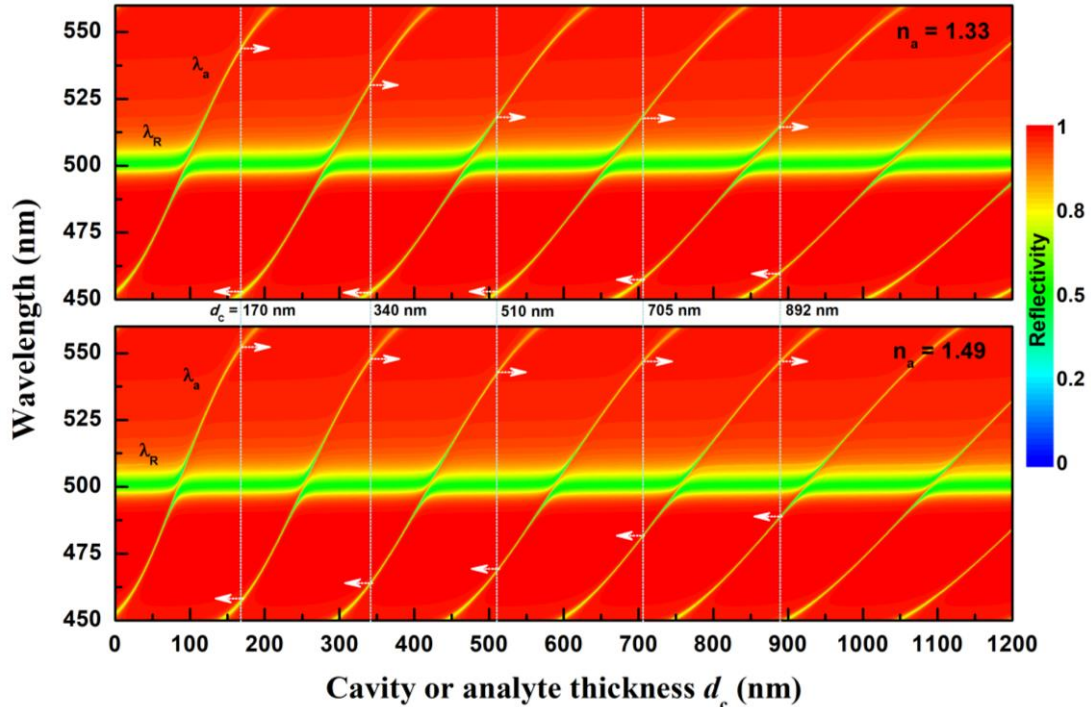


Fig. 7. Reflectivity contour as a function of wavelength and cavity or analyte thickness d_c for two different values of refractive index of analyte: $n_a = 1.33$ and 1.49 , respectively in a hybrid structure of $\text{MS}(\text{HL})^N\text{C}(\text{HL})^N$ with $(\text{HL})^N = (\text{HfO}_2/\text{SiO}_2)^{10}$. The cavity layer C has been filled with analyte. The modes splitting has been found at the strong coupling region for different values of cavity thickness. For cavity thickness values other than strong coupling region, the reference mode λ_R remains unchanged, while the analyte mode λ_a shifts. Such cavity thickness values can be selected for self-referenced sensing applications. Here, 5-values of cavity thickness $d_c=170$ nm, 340 nm, 510 nm, 705 nm, and 892 nm, which lie in the weak coupling region, are selected for example purposes. The arrow

indicated towards right side in the plot represents λ_a above λ_R , while the arrow directed towards left side represents λ_a below λ_R . One can clearly see the shifting of both lower and upper analyte mode with varying refractive index of analyte from 1.33 to 1.49 for the selected values of cavity thickness, which is explored for refractive index sensing application.

In the present study, we have used analyte resonant mode λ_a above λ_R for refractive index sensing application. Subsequently, the reflectivity spectra for both structures S1 and S2 with varying refractive index of analytes in the range 1.33-1.49 have been calculated for the above mentioned five different cavity thickness values and plotted in Fig. 8(a) and (b), respectively. The wider wavelength range reflectivity spectra that exhibit multiple analyte modes (one above λ_R and other below λ_R) with varying refractive index of analyte and cavity thickness are provided in the supplementary material [see Fig. S6]. It can be clearly seen that the reflectivity dip due to the mode λ_R remains unchanged with varying analyte refractive index. On the contrary, the reflectivity dip (R_a) at the resonant analyte mode λ_a undergoes significant shift as a function of refractive index of the analytes filled in the cavity. This makes it useful for designing “self-referencing sensor”, where λ_R becomes the reference mode and remains fixed, while λ_a shifts considerably with varying optical properties (refractive index) of the cavity medium. It is worthy to note that the shift of λ_a with respect λ_R becomes larger with increasing cavity thickness d_c in both structures S1 and S2. It is found that further increase of cavity thickness generates additional resonant modes within the PBG, consequently the design of the sensor becomes complex. Moreover, this could lead to shift of λ_a near the edge of the PBG that would badly affect the signal to noise ratio (SNR) of the sensor. Therefore, only five optimized cavity thickness values are chosen for the present proposed sensors.

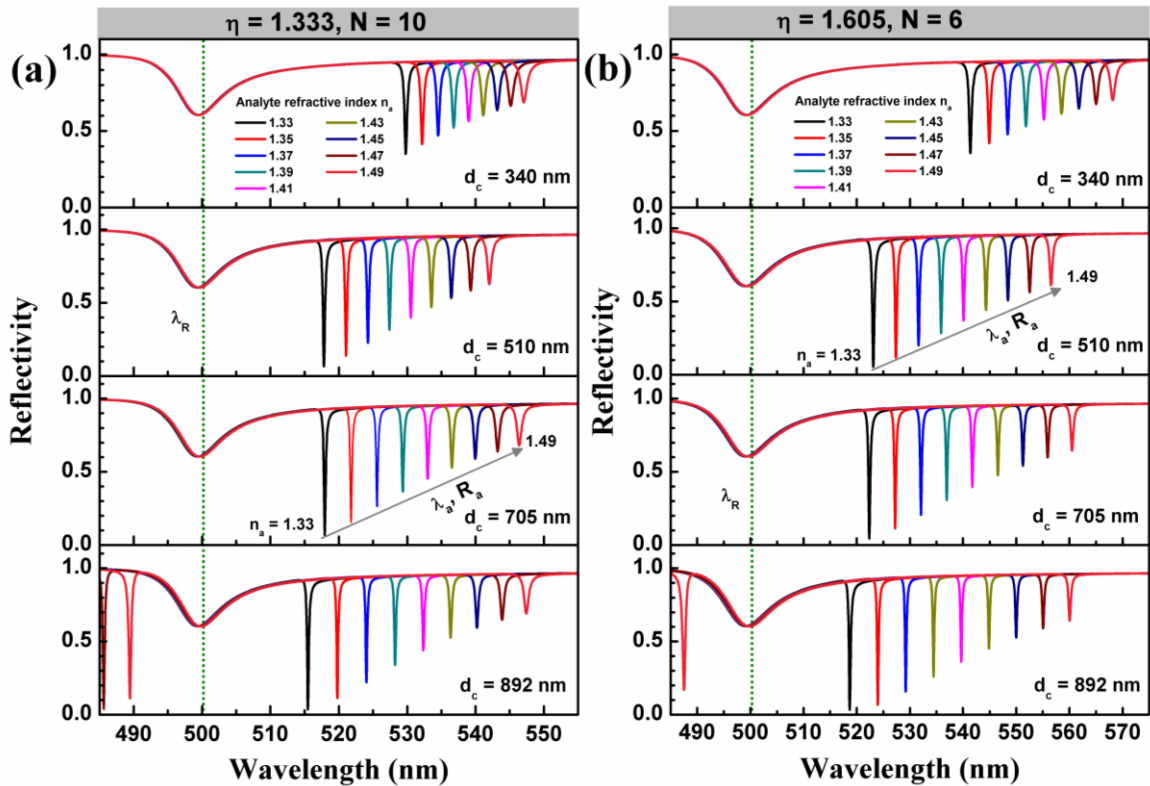


Fig. 8. Reflectivity spectra with varying refractive index values of analyte filled in the cavity in the hybrid structures $MS(HL)^N C(HL)^N$ with $(HL)^N$ as (a) $(HfO_2/SiO_2)^{10}$ 1DPC with refractive index contrast

$\eta=1.333$ and number of periods $N=10$ [structure S1], and (b) $(\text{TiO}_2/\text{SiO}_2)^6$ 1DPC with $\eta=1.605$ and $N=6$ [structure S2], for different values of cavity or analyte thickness: $d_c=170$ nm, 340 nm, 510 nm, 705 nm, and 892 nm.

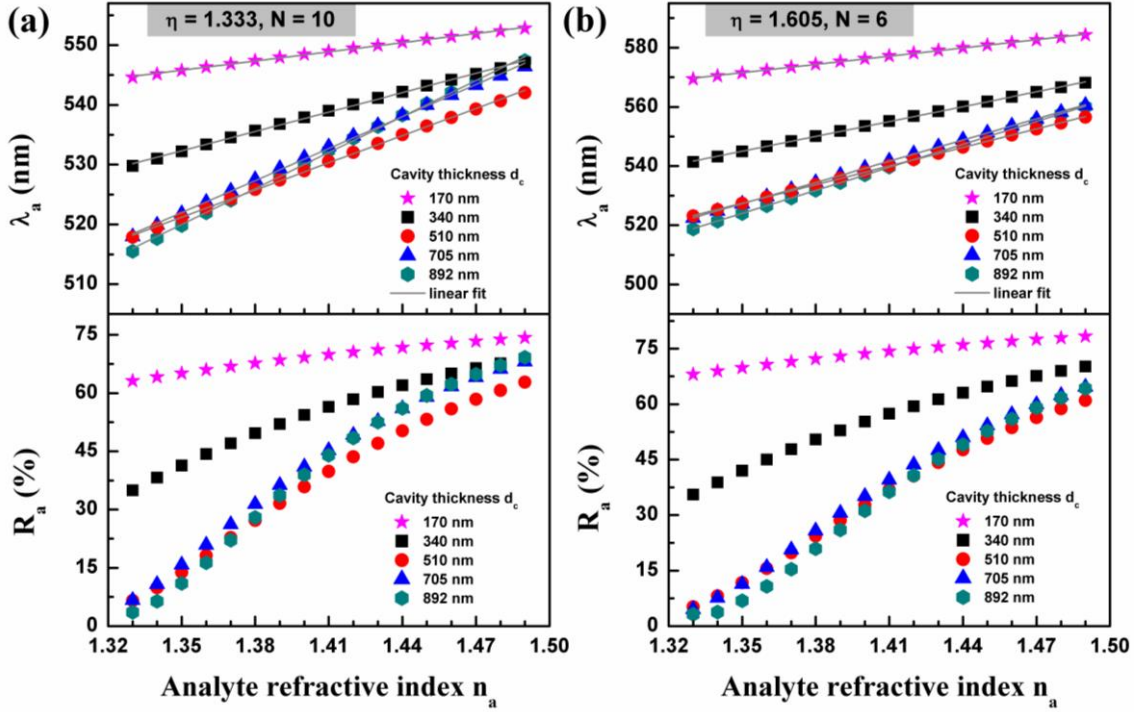


Fig. 9. Position of analyte mode wavelength (λ_a) and reflectivity minimum (R_a) at λ_a as a function of analyte refractive index for the hybrid structures (a) S1 and (b) S2 for different cavity thicknesses.

The values of λ_a and R_a with varying analyte medium for different cavity thickness are plotted in Fig. 9 (a) and (b) for the structures S1 and S2, respectively. The value of λ_a shifts to longer wavelength and the value of reflectivity dip R_a increases with increasing refractive index of the analyte which suggests that either of change in λ_a and R_a or both can be used for the refractive index sensing application. The change in both λ_a and R_a is maximum for cavity thickness of 892 nm in both the structures. Such significant changes could be understood by analysing the electric field distribution of λ_a . For better visualisation and understanding of electric field intensity in the hybrid structure, the cavity or analyte layer centre is considered as $z=0$ for the electric field calculations. The analyte mode electric field distribution has been plotted for different values of analyte index $n_a=1.35, 1.40$, and 1.45 in Fig. 10(a) for a fixed value of $d_c=340$ nm and $\eta=1.333$. It shows that the electric field within the analyte layer around $z=0$ gets enhanced by close to four times with decreasing the analyte index from 1.45 to 1.35, which indicates that the cavity/analyte mode would exhibit better quality factor for low index analyte as compared to that of high index analyte. The analyte mode field distribution with varying thickness of cavity or analyte layer has been plotted in Fig. 10(b) for a fixed value of $n_a=1.35$ and $\eta=1.333$. It shows that the field gets much stronger and more localized with increasing cavity thickness from 170 nm to 510 nm. As a result, the bandwidth of the analyte mode will be narrower and the dip reflectivity will be dipper with increasing cavity thickness. This in turn improves the sensitivity and quality factor of the analyte mode. Fig. 10(c) shows

the mode field distribution for two different values of refractive index contrast $\eta=1.333$ and 1.605 in the 1DPC. The mode field is much stronger and confined in higher index contrast photonic structure. The electric field intensity becomes ten times by increasing index contrast from 1.333 to 1.605 , which confirms the increasing sensitivity of the analyte modes in case of higher index contrast structure. The change in electric field distribution in all the considered cases is significant, which is essentially the prime reason behind such large shift of the resonant analyte mode λ_a as observed in Fig. 8. In all cases, the electric field is seen amplified also in the two 1DPC structures besides the amplification in the cavity. Because, the presence of metallic layer and 1DPC makes the whole structure like a Fabry-Perot cavity resulting resonances both in the cavity and in the two 1DPCs. The strong amplification of electric field leads to high Q value for the coupled modes.

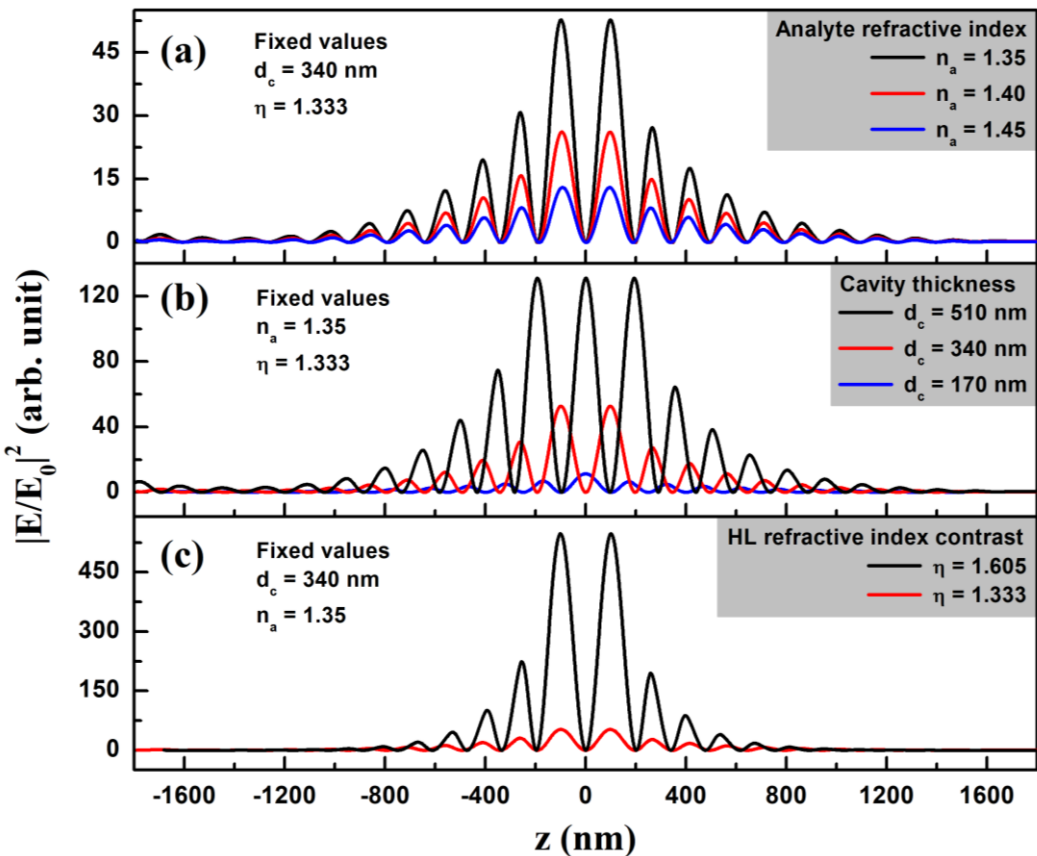


Fig. 10. Electric field distribution of the analyte modes in the hybrid structure for (a) different refractive index values of the analyte n_a with a fixed value of d_c and η , (b) for different values of the cavity thickness d_c with a fixed value of n_a and η , and (c) for different values of refractive index of the 1DPC η with a fixed value of d_c and n_a .

Now, the performance of the hybrid modes-based sensor for both the structure S1 and S2 has been evaluated by analyzing the shift of λ_a . The sensitivity S_n of the sensor is defined as $S_n = \Delta\lambda_a / \Delta n_a$, where $\Delta\lambda_a$ is the shift of the analyte mode and Δn_a is the change in refractive index of the analyte (cavity medium). Sensitivity has been obtained from the slope of the plots λ_a vs. n_a in Fig. 8. The derived sensitivity of both structures S1 and S2 as a function of cavity thickness are shown in Fig. 9. The sensitivity is found increasing from 51 nm/RIU to 201 nm/RIU and 93 nm/RIU to 259 nm/RIU with increasing cavity thickness from 170 nm to 892

nm for the structures S1 and S2, respectively. The sensitivity obtained for both the structures is better than that of the previously reported values [22, 24] for the TP based sensors. The structure S2 has better sensitivity than S1. It clearly indicates that hybrid plasmonic-1D photonic crystal structure made of dielectric materials with wider refractive index contrast gives better sensitivity. Moreover, wider the index contrast η , lesser number of periods N is required to achieve the desired PBG. The maximum sensitivity obtained for the structure S2 is 259 nm/RIU, which is much better than various photonic crystal-fiber based interferometric sensors [38], and recently reported TP mode based mesoporous multilayer sensor [39]. Though, the sensitivity of SPR based sensor remains ahead as compared to the proposed hybrid structure-based sensor which is primarily due to polarization dependent strong dispersive nature of SPR mode. However, the sensing configuration of hybrid mode-based sensor is much easier than that of SPR sensors.

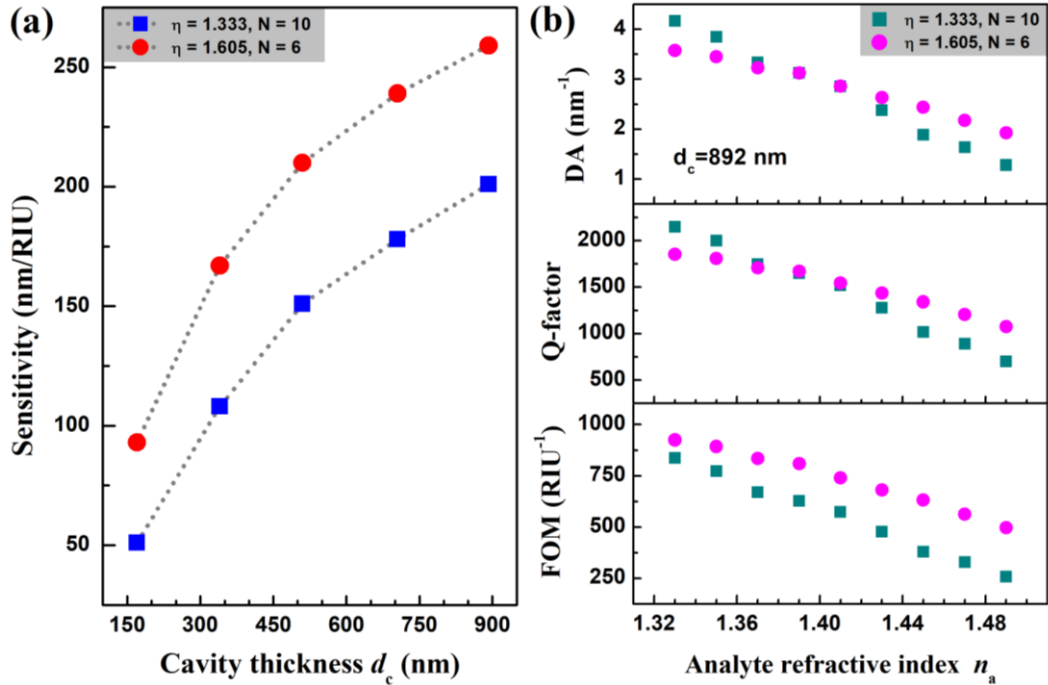


Fig. 11. (a) Sensitivity of the hybrid photonic structures S1 and S2 as a function of cavity thickness. (b) DA, Q-factor, and FOM for both structures as a function of refractive index of the analyte for a fixed value of cavity thickness of 892 nm.

Other than sensitivity, detection accuracy (DA), quality factor (Q-factor), and figure of merit (FOM) are also vital parameters that decide the performance of the sensor and are expressed as follows: $DA = 1 / \delta_a$, $Q\text{-factor} = \lambda_a / \delta_a$, and $FOM = S_n / \delta_a$, where δ_a is the fullwidth at half minima of the reflection dip corresponding to the analyte mode λ_a . These expressions indicate that sharper resonant modes improve the overall performance of the sensors. The value of DA, Q-factor, and FOM has been found decreasing with increasing refractive index of the analyte. The variation of such parameters for sensor structures of S1 and S2 with maximum sensitivity (for cavity thickness of 892 nm) are plotted in Fig. 10(b) as a representative plot. The value of DA decreases from 4.16 nm^{-1} to 1.28 nm^{-1} for S1, and 3.57 nm^{-1} to 1.92 nm^{-1} for S2 with increasing n_a from 1.33 to 1.49. The obtained DA is much better

than that obtained in case of SPR sensors. The typical *DA* for SPR sensors is around 0.02 nm^{-1} in the visible region which is due to the involvement of additional dispersion compensating components (prisms and gratings) for exciting the SPR mode. The *Q*-factor decreases from 2148 to 701 for S1, and 1852 to 1077 for S2 with increasing n_a from 1.33 to 1.49. The *FOM* decreases from 837 RIU-1 to 258 RIU $^{-1}$ for S1, and 925 RIU-1 to 498 RIU $^{-1}$ for S2 with increasing analyte index in the given range. It is observed that the *DA* and *Q*-factor of the sensor made of structure S1 is better than that of S2 for the refractive index of the analyte in the range 1.33 to 1.37, while it is reverse for $n_a > 1.37$. The *DA* and *Q*-factor of structure S2 can be better than that of S1 in the whole range of refractive index of the analyte if *N* could be chosen larger. Overall, structure S2 exhibits better sensing performance than that of S1. It is worth to mention here that the value of *DA*, *FOM*, and *Q*-factor of the structure S2 could be further improved by increasing the number of periods *N* as it will drastically narrow the FWHM of the reflection dip. This confirms that the performance of the hybrid plasmonic-photonic structure-based sensors can be further improved by optimizing number of periods *N* and/or thickness of metal and spacer layers, and choosing high refractive index contrast η dielectric materials for 1DPC. This proposed hybrid photonic structure will be much easier to configure for a sensor as the hybrid modes are polarisation insensitive and the light can be easily coupled to the structure in free space to excite the modes for index sensing application.

4. Conclusion

Rabi-like splitting and self-referenced refractive index sensing in Ag/1DPC/cavity/1DPC structures has been realized due to the coupling between Tamm plasmon mode and cavity mode. It is found that Rabi-like splitting energy is tunable by either varying *N* for a fixed η or varying η for a fixed *N*. The polarization splitting of one of the hybrid modes is much higher as compared to that of other mode. The modes coupling changes by varying thickness and refractive index of the analyte medium in the cavity in which the value of resonant reflectivity and the corresponding wavelength of one of the modes remains unchanged while that of the other mode undergoes significant change, therefore the structure acts as a self-referenced refractive index sensor for a fixed cavity thickness. The response of the two proposed hybrid structure sensors is linear for the analytes in the refractive index range of 1.33 to 1.49. The structures made of $\eta=1.605$ and *N*=6 shows better sensing performance as compared to that made of $\eta = 1.333$ and *N*=10. The sensitivity of the sensor ($\eta=1.605$ and *N*=6) is comparable to that of fibre interferometer sensors and SPR sensors. Moreover, the thickness of cavity (sensing) medium in the proposed structure has been made close to 900 nm which is much larger than that of the reported values so far for the TP based sensors. The larger thickness of sensing medium not only improves its sensitivity but also makes the hybrid structure more practically feasible. The proposed structures can be used for chemical or biochemical sensing by integrating nano/microfluidic channel in the hybrid plasmonic-photonic crystals.

References

- [1] M. Kaliteevski, I. Iorsh, S. Brand, R. Abram, J. Chamberlain, A. Kavokin, I. Shelykh, Tamm plasmon-polaritons: Possible electromagnetic states at the interface of a metal and a dielectric Bragg mirror, *Physical Review B*, 76 (2007) 165415.
- [2] M. Sasin, R. Seisyan, M. Kaliteevski, S. Brand, R. Abram, J. Chamberlain, A.Y. Egorov, A. Vasil'Ev, V. Mikhlin, A. Kavokin, Tamm plasmon polaritons: Slow and spatially compact light, *Applied physics letters*, 92 (2008) 251112.
- [3] P.S. Pankin, S.Y. Vetrov, I.V. Timofeev, Tunable hybrid Tamm-microcavity states, *JOSA B*, 34 (2017) 2633-2639.
- [4] M.V. Pyatnov, S.Y. Vetrov, I.V. Timofeev, Localized optical modes in a defect-containing liquid-crystal structure adjacent to the metal, *JOSA B*, 34 (2017) 2011-2017.
- [5] Z. Wang, J.K. Clark, Y.-L. Ho, B. Vilquin, H. Daiguji, J.-J. Delaunay, Narrowband thermal emission from Tamm plasmons of a modified distributed Bragg reflector, *Applied Physics Letters*, 113 (2018) 161104.
- [6] A.M. Ahmed, A. Mehaney, Ultra-high sensitive 1D porous silicon photonic crystal sensor based on the coupling of Tamm/Fano resonances in the mid-infrared region, *Scientific reports*, 9 (2019) 1-9.
- [7] Z.A. Zaky, A.M. Ahmed, A.S. Shalaby, A.H. Aly, Refractive index gas sensor based on the Tamm state in a one-dimensional photonic crystal: theoretical optimisation, *Scientific reports*, 10 (2020) 1-9.
- [8] P. Das, S. Mukherjee, M. Wan, S.K. Ray, Optical Tamm state aided room-temperature amplified spontaneous emission from carbon quantum dots embedded one-dimensional photonic crystals, *Journal of Physics D: Applied Physics*, 52 (2018) 035102.
- [9] N. Lundt, S. Klembt, E. Cherotchenko, S. Betzold, O. Iff, A.V. Nalitov, M. Klaas, C.P. Dietrich, A.V. Kavokin, S. Höfling, Room-temperature Tamm-plasmon exciton-polaritons with a WSe₂ monolayer, *Nature communications*, 7 (2016) 1-6.
- [10] J. Hu, E. Yao, W. Xie, W. Liu, D. Li, Y. Lu, Q. Zhan, Strong longitudinal coupling of Tamm plasmon polaritons in graphene/DBR/Ag hybrid structure, *Optics express*, 27 (2019) 18642-18652.
- [11] Z. Wang, J.K. Clark, Y.-L. Ho, B. Vilquin, H. Daiguji, J.-J. Delaunay, Narrowband thermal emission realized through the coupling of cavity and Tamm plasmon resonances, *ACS photonics*, 5 (2018) 2446-2452.
- [12] H. Lu, Y. Li, H. Jiao, Z. Li, D. Mao, J. Zhao, Induced reflection in Tamm plasmon systems, *Optics Express*, 27 (2019) 5383-5392.
- [13] R.V. Nair, The interaction between optical Tamm state and microcavity mode in a planar hybrid plasmonic-photonic structure, *Photonics and Nanostructures - Fundamentals and Applications*, 36 (2019) 100702.
- [14] F.H. Alast, G. Li, K. Cheah, Rabi-like splitting from large area plasmonic microcavity, *AIP Advances*, 7 (2017) 085201.
- [15] G. Khitrova, H. Gibbs, M. Kira, S.W. Koch, A. Scherer, Vacuum Rabi splitting in semiconductors, *Nature Physics*, 2 (2006) 81-90.
- [16] L. Zhang, Y. Zhang, Y. Zhao, J. Zhai, L. Li, Rabi splitting induced by a metamaterial plasmon cavity, *Optics express*, 18 (2010) 25052-25060.

- [17] S. Chen, G. Li, D. Lei, K.W. Cheah, Efficient energy exchange between plasmon and cavity modes via Rabi-analogue splitting in a hybrid plasmonic nanocavity, *Nanoscale*, 5 (2013) 9129-9133.
- [18] P. Das, S. Mukherjee, S. Jana, S.K. Ray, B.S. Bhaktha, Resonant and non-resonant coupling of one-dimensional microcavity mode and optical Tamm state, *Journal of Optics*, 22 (2020) 065002.
- [19] R. Brückner, M. Sudzius, S. Hintschich, H. Fröb, V. Lyssenko, K. Leo, Hybrid optical Tamm states in a planar dielectric microcavity, *Physical Review B*, 83 (2011) 033405.
- [20] M. Maragkou, C.E. Richards, T. Ostatnický, A.J. Grundy, J. Zajac, M. Hugues, W. Langbein, P.G. Lagoudakis, Optical analogue of the spin Hall effect in a photonic cavity, *Optics letters*, 36 (2011) 1095-1097.
- [21] C. Symonds, A. Lemaître, E. Homeyer, J. Plenet, J. Bellessa, Emission of Tamm plasmon/exciton polaritons, *Applied Physics Letters*, 95 (2009) 151114.
- [22] P.S. Maji, M.K. Shukla, R. Das, Blood component detection based on miniaturized self-referenced hybrid Tamm-plasmon-polariton sensor, *Sensors and Actuators B: Chemical*, 255 (2018) 729-734.
- [23] M. Shaban, A.M. Ahmed, E. Abdel-Rahman, H. Hamdy, Tunability and sensing properties of plasmonic/1D photonic crystal, *Scientific reports*, 7 (2017) 1-10.
- [24] S. Kumar, M.K. Shukla, P.S. Maji, R. Das, Self-referenced refractive index sensing with hybrid-Tamm-plasmon-polariton modes in sub-wavelength analyte layers, *Journal of Physics D: Applied Physics*, 50 (2017) 375106.
- [25] L.A. Pettersson, L.S. Roman, O. Inganäs, Modeling photocurrent action spectra of photovoltaic devices based on organic thin films, *Journal of Applied Physics*, 86 (1999) 487-496.
- [26] C.C. Katsidis, D.I. Siapkas, General transfer-matrix method for optical multilayer systems with coherent, partially coherent, and incoherent interference, *Applied optics*, 41 (2002) 3978-3987.
- [27] E. Centurioni, Generalized matrix method for calculation of internal light energy flux in mixed coherent and incoherent multilayers, *Applied Optics*, 44 (2005) 7532-7539.
- [28] H.A. Macleod, *Thin-film optical filters*, CRC press2017.
- [29] S. Larouche, L. Martinu, OpenFilters: open-source software for the design, optimization, and synthesis of optical filters, *Applied optics*, 47 (2008) C219-C230.
- [30] P. Peumans, A. Yakimov, S.R. Forrest, Small molecular weight organic thin-film photodetectors and solar cells, *Journal of Applied Physics*, 93 (2003) 3693-3723.
- [31] J. Hu, W. Liu, W. Xie, W. Zhang, E. Yao, Y. Zhang, Q. Zhan, Strong coupling of optical interface modes in a 1D topological photonic crystal heterostructure/Ag hybrid system, *Opt. Lett.*, 44 (2019) 5642-5645.
- [32] Y.-t. Fang, L.-x. Yang, W. Kong, N. Zhu, Tunable coupled states of a pair of Tamm plasmon polaritons and a microcavity mode, *Journal of Optics*, 15 (2013) 125703.
- [33] M. Kaliteevski, S. Brand, R. Abram, I. Iorsh, A. Kavokin, I. Shelykh, Hybrid states of Tamm plasmons and exciton polaritons, *Applied Physics Letters*, 95 (2009) 251108.

- [34] R. Brückner, M. Sudzius, S. Hintschich, H. Fröb, V. Lyssenko, M. Kaliteevski, I. Iorsh, R. Abram, A. Kavokin, K. Leo, Parabolic polarization splitting of Tamm states in a metal-organic microcavity, *Applied Physics Letters*, 100 (2012) 062101.
- [35] K.V. Sreekanth, Y. Alapan, M. ElKabbash, E. Ilker, M. Hinczewski, U.A. Gurkan, A. De Luca, G. Strangi, Extreme sensitivity biosensing platform based on hyperbolic metamaterials, *Nature materials*, 15 (2016) 621-627.
- [36] A. Salim, S. Lim, Review of recent metamaterial microfluidic sensors, *Sensors*, 18 (2018) 232.
- [37] X. Liang, K.J. Morton, R.H. Austin, S.Y. Chou, Single sub-20 nm wide, centimeter-long nanofluidic channel fabricated by novel nanoimprint mold fabrication and direct imprinting, *Nano letters*, 7 (2007) 3774-3780.
- [38] R. Jha, J. Villatoro, G. Badenes, Ultrastable in reflection photonic crystal fiber modal interferometer for accurate refractive index sensing, *Applied Physics Letters*, 93 (2008) 191106.
- [39] B. Auguié, M.C. Fuertes, P.C. Angelomé, N.L. Abdala, G.J. Soler Illia, A. Fainstein, Tamm plasmon resonance in mesoporous multilayers: toward a sensing application, *Acs Photonics*, 1 (2014) 775-780.

Supplementary material

Rabi-like splitting and refractive index sensing with hybrid Tamm plasmon-cavity modes

S. Jena*, R. B. Tokas, S. Thakur, and D. V. Udupa

Atomic & Molecular Physics Division, Bhabha Atomic Research Centre, Mumbai 400 085, India

Coupling of modes without spacing layer:

Top plot of Fig. S1 shows the bare cavity mode in the structure $(HL)^5C(HL)^5$. The middle plot of Fig. S1 is the TP mode at lower energy region in the structure $M(HL)^{10}$, which is originated due to the electric field localized next to the metallic layer. Combining above two structures leads to $M(HL)^5C(HL)^5$ and it exhibits both the modes as shown in the bottom plot of Fig. S1. But one of the modes undergoes red-shift and it is the TP mode. Here, the modes are clearly distinguishable as they are poorly coupled. It can be clearly seen that the modes are weakly coupled in the absence of spacing layer. Therefore, spacing layer is essential for strong coupling of the modes as detailed in the main manuscript.

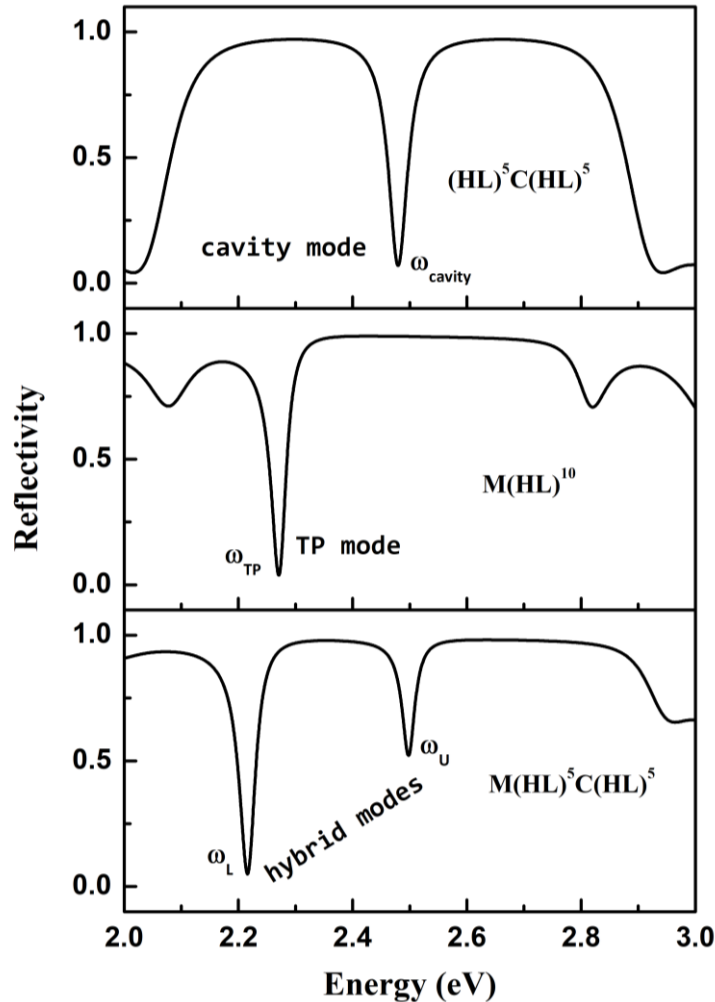


Fig. S1. Hybrid $M(HL)^5C(HL)^5$ structure without spacing S layer: Reflection spectra of the photonic structure without metallic M layer (bare cavity mode), without cavity C layer (bare TP mode), and with both M and C layers (hybrid TP-cavity modes), respectively.

Optimization of plasmonic layer thickness:

Fig. S2 shows that TP mode exists in both the structures for a specific range of values of d_m . In case of $MS(HL)^{10}$, the d_m values lies in the range 40-75 nm, while it is in the range 30-50 nm for the $MS(HL)^5C(HL)^5$ hybrid photonic structure. Therefore, optimized value of d_m should be chosen for the desired coupling of the TP mode with the cavity mode, which is 35 nm in the present study. Correlating Fig. S2(b) with Fig. S2(a), it can be inferred that the energy $\omega_U=2.541$ eV corresponds to the cavity mode part whereas the energy $\omega_L=2.416$ eV corresponds to TP mode part in the hybrid TP-cavity modes.

*High index thin layer H [$n_H=1.96$]

*Low index thin layer L [$n_L=1.47$]

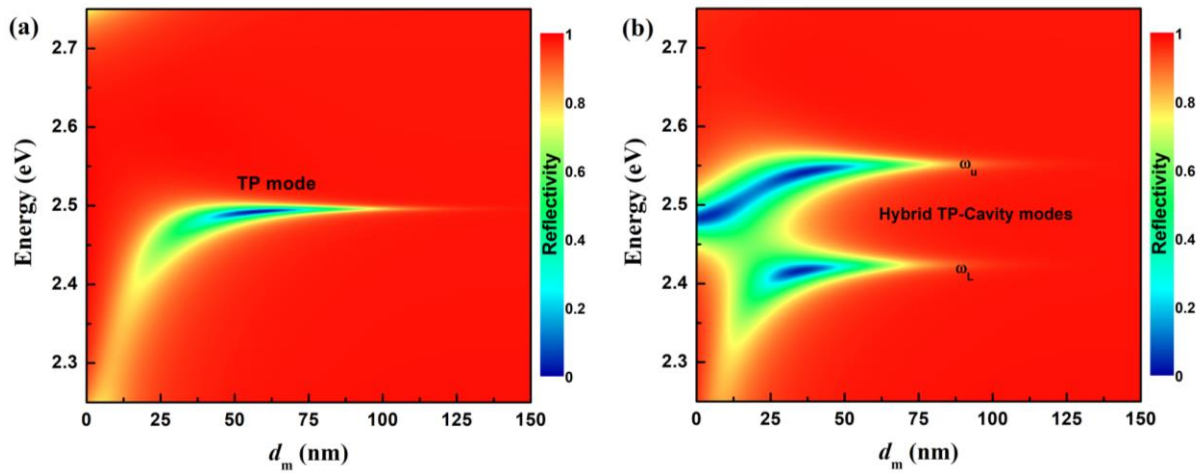


Fig. S2. Reflectivity spectra as a function of metallic M layer thickness (d_m) for (a) $MS(HL)^{10}$, and (b) $MS(HL)^5C(HL)^5$ photonic structure, respectively.

Effect of spacing layer thickness on bare mode and hybrid modes:

Fig. S3 illustrates the effect of spacer layer thickness (d_s) on the bare modes and coupled hybrid modes. It is seen that the bare cavity mode does not change with varying S layer thickness, while the bare TP mode undergoes redshift with increasing d_s . In case of hybrid structure, the coupled modes deviate from their bare TP and cavity modes in the strong coupling region *i.e.* $130 \text{ nm} \leq d_s \leq 150 \text{ nm}$, and behave like bare modes in either side of the strong coupling region. The TP and the cavity mode repel each other strongly away from their unique uncoupled mode energy at $d_s=141 \text{ nm}$, which results to the anticrossing of the two modes when they approach each other. This anticrossing is the signature of strong coupling. Therefore, the optimized thickness of S layer that is responsible for strong coupling of modes is 141 nm.

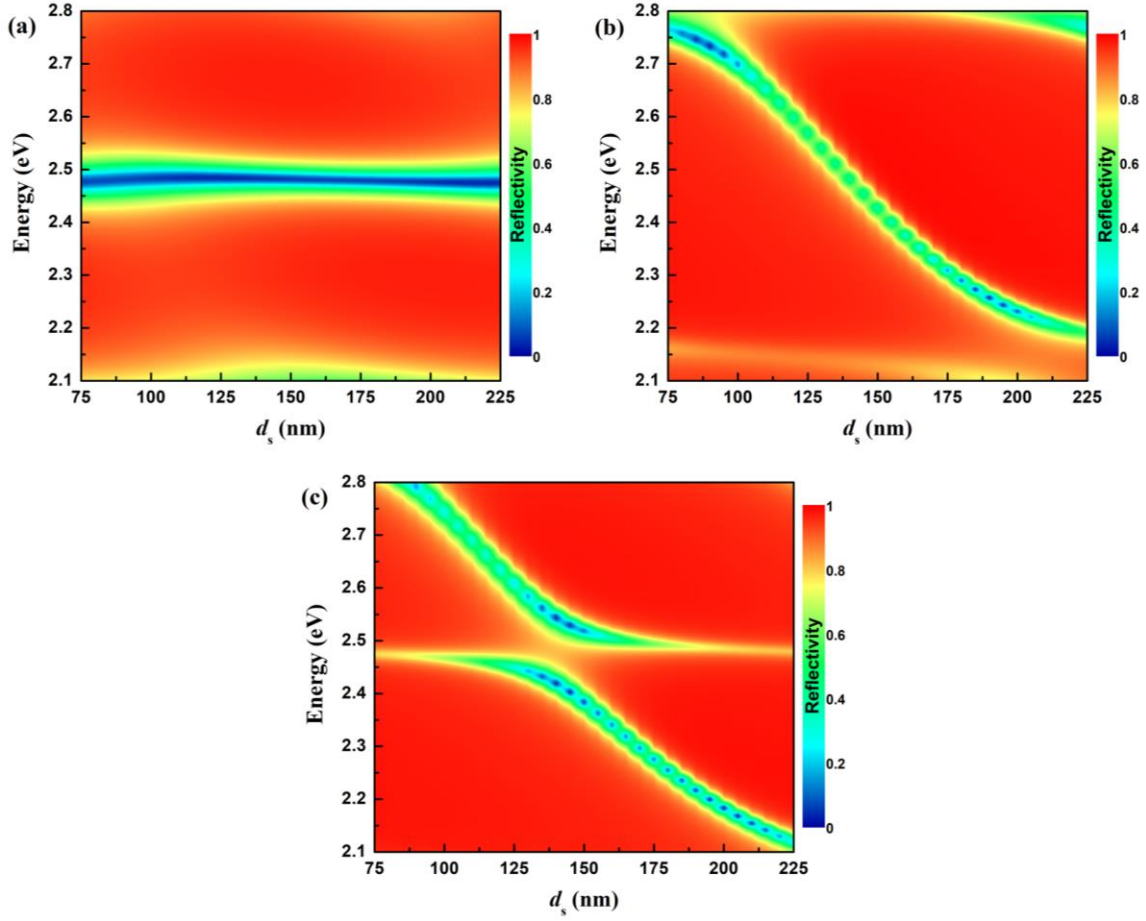


Fig. S3. Reflectivity contour as a function of incident light energy and S layer thickness d_s for (a) $(HL)^5C(HL)^5$, (b) $MS(HL)^{10}$, and (c) $MS(HL)^5C(HL)^5$ photonic structure, respectively.

Reflectivity of hybrid modes with varying N:

Fig. S4 shows that the cavity mode shifts to higher wavelength and its linewidth becomes wider with increasing value of n_a , while the TP mode remains unchanged. The refractive index of analyte is varied from 1.33 to 1.49 with an interval of $\Delta n=0.04$. With increasing N, the linewidth of the cavity mode gets sharper that increases its Q-factor. For lower N value, the modes are weakly localized as a result the reflectivity dip linewidth gets wider and the resonant TP mode changes with varying N. Therefore, such low N structures can no longer be useful for making sensors. For higher N value, the TP mode gets strongly localized as a result the corresponding dip reflectivity and wavelength values remain unchanged for higher value of N and it acts as a reference. Therefore, the hybrid structure can be used for self-referenced refractive index sensing.

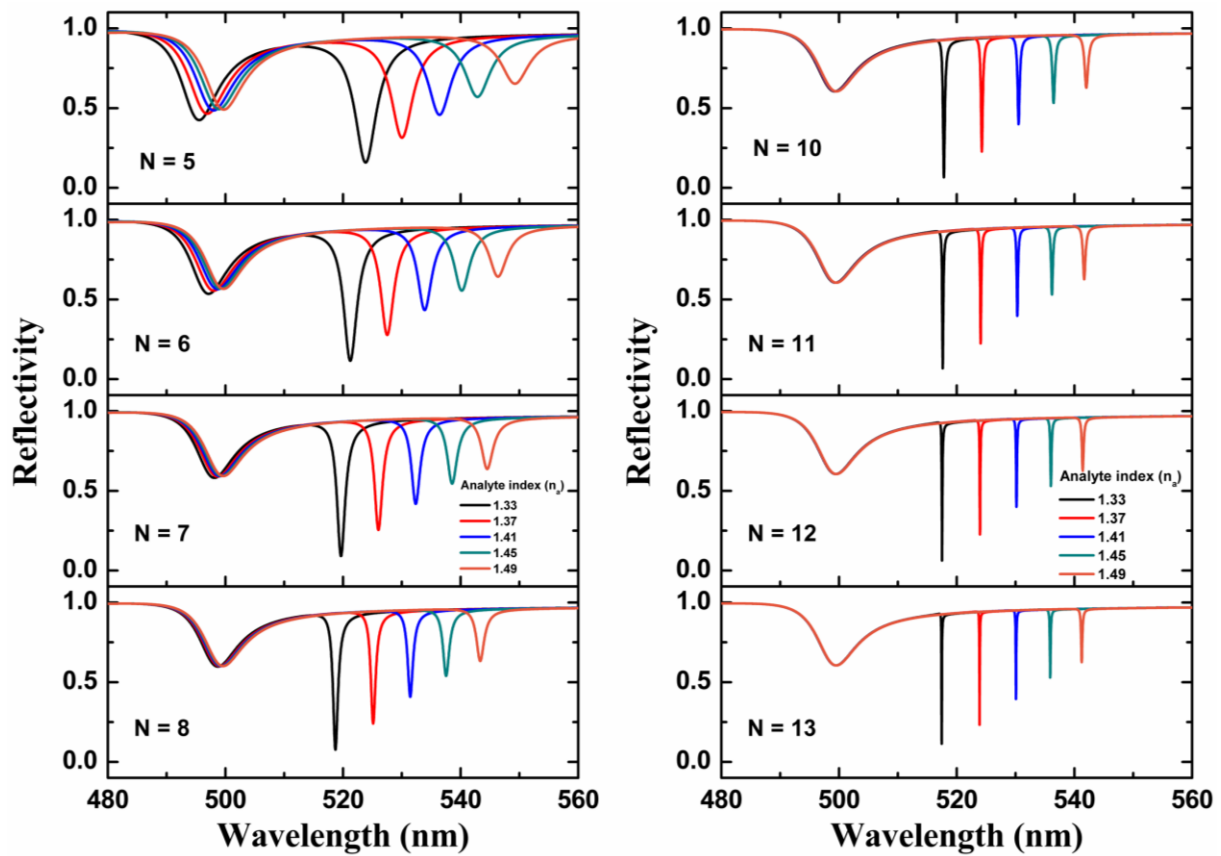


Fig. S4. Reflection spectra of the hybrid photonic structure with varying analytes refractive index (n_a) in the cavity layer as a function of number of period N .

Reflectivity of $\text{Ag}/\text{SiO}_2/(\text{TiO}_2/\text{SiO}_2)^6/\text{C}/(\text{TiO}_2/\text{SiO}_2)^6$ with varying cavity thickness for two analyte indices $n_a=1.33$ and 1.49 :

In Fig. S5, the cavity layer C can be filled with different analytes. Here, we have only considered two analytes having extreme refractive index values $n_a=1.33$ and 1.49 . The figure shows that the coupling of modes depends on cavity thickness and there exists several values of cavity thickness for which the modes get strongly coupled and deviate from each other. Therefore, such thickness values should be avoided for sensing applications as both the coupled modes shifts their positions with varying analyte medium. For cavity thickness values other than strong coupling region, the reference mode λ_R remains unchanged, while the analyte mode λ_a shifts. Such cavity thickness values can be selected for self-referenced sensing applications. Here, 5-values of cavity thickness $d_c=170$ nm, 340 nm, 510 nm, 705 nm, and 892 nm, which lie in the weak coupling region, are selected for example purposes. The arrow indicated towards right side in the plot represents λ_a above λ_R , while the arrow directed towards left side represents λ_a below λ_R . One can clearly see the shifting of both lower and upper analyte mode with varying refractive index of analyte from 1.33 to 1.49 for the selected values of cavity thickness, which is explored for refractive index sensing application.

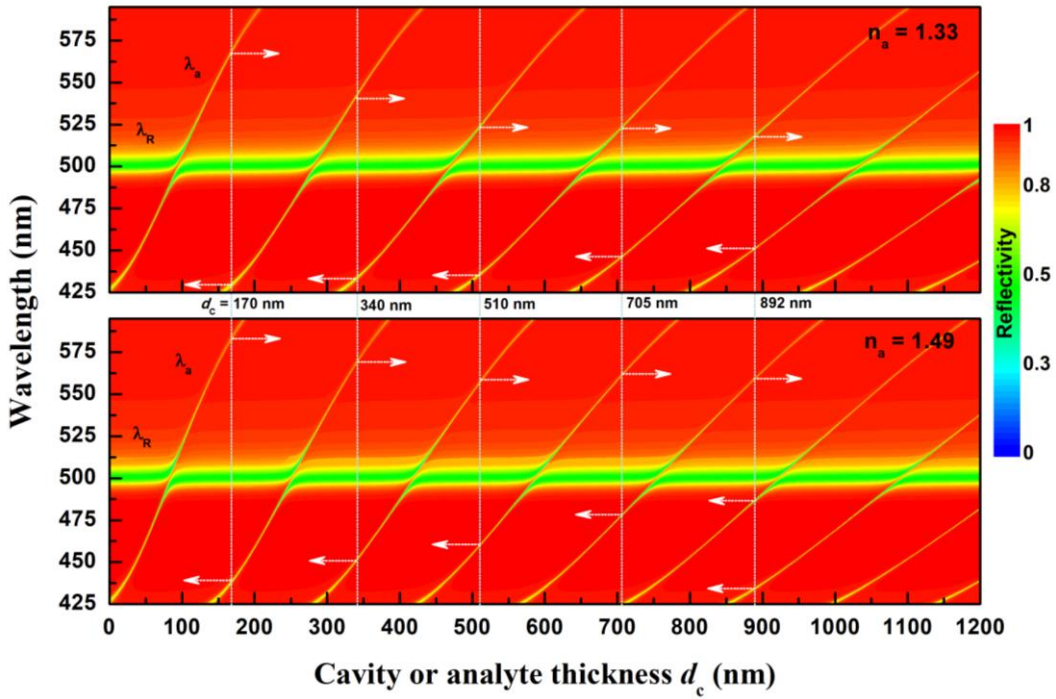


Fig. S5. Reflectivity contour as a function of wavelength and cavity or analyte thickness d_c for two different values of refractive index of analyte: $n_a = 1.33$ and 1.49 , respectively in a hybrid structure of $MS(HL)^N C(HL)^N$ with $(HL)^N = (TiO_2/SiO_2)^6$.

Reflectivity of two hybrid structures S1 and S2 for wide spectral range:

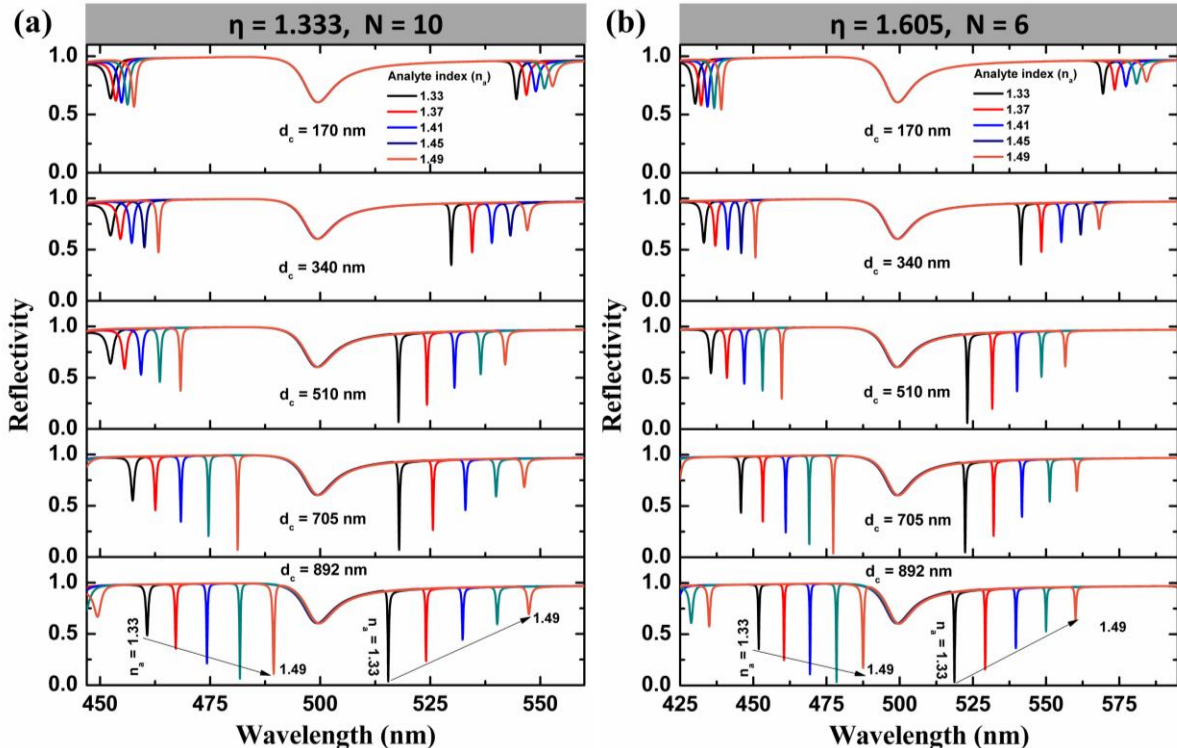


Fig. S6. Wider spectral reflectivity of hybrid structures S1 and S2 with varying refractive index of analyte filled in the cavity for different cavity thicknesses. Cavity mode either above or below TP mode can be used for sensing application.